Effects of long-range repulsive interactions on Ostwald ripening

Celeste Sagui and Rashmi C. Desai
Department of Physics, University of Toronto, Toronto, Ontario, Canada M5S 1A7
(Received 27 February 1995)

The effects of a long-range repulsive interaction on the phenomena of Ostwald ripening are studied. Beginning with a Langevin description, interface equations describing both the growth and motion of droplets are derived and solved numerically. Two noncoarsening and one coarsening regimes are found. In the noncoarsening regimes, if the system is allowed to reach hexagonal order, the droplet distribution function approaches a δ function; if hexagonal order is somehow precluded, the system becomes kinetically frozen. In the coarsening regime, the mean radius of droplets grows in time. In both the kinetically frozen and coarsening regimes, the system is disordered and polydisperse with a strong coupling between the position and the size of the droplets.

PACS number(s): 68.45.Da, 68.10.Jy, 82.70.−y, 83.70.Hq

I. INTRODUCTION

The classic work of Lifshitz, Slyozov, and Wagner [1,2] presented the definitive theory of coarsening process in a binary mixture in the limit of zero volume fraction. The coarsening process, which is also referred to as Ostwald ripening, is the process by which droplets of a minority phase in a binary mixture evolve during the late stages of phase separation. During the coarsening, material from small, high-curvature droplets evaporates, diffuses through the matrix, and condenses on the larger, low-curvature droplets. The system reduces its total interfacial free energy by making large droplets grow at the expense of the smaller ones, while maintaining local equilibrium. Lifshitz, Slyozov, and Wagner showed that a scaling regime is reached during which the mean droplet radius increases as a power law with growth exponent of 1/3. They also derived an expression for the scaled droplet distribution function. During the past three decades, there has been extensive experimental, analytical, and numerical work on the Lifshitz-Slyozov-Wagner (LSW) mechanism [3]; much of the recent work is focused on the corrections to the scaled distribution function due to nonzero volume fractions.

Since the binary mixtures considered above exemplify systems with a conserved order parameter and attractive interactions only, the LSW theory becomes inapplicable to a wide variety of materials with both short-range attractive and effective long-range repulsive interactions (LRRI's). These competing interactions lead to the formation of a rich variety of spatially modulated phases, termed supercrystals. Spatial modulations in the corresponding order parameter field reduce the energy originating from the LRRI. The system forms domains, defined as regions of uniform amplitude of the order parameter, separated from one another by domain boundaries or walls. These domains arrange themselves in certain geometrical symmetries (the supercrystal phases) that depend on the parameters of the LRRI, the average order parameter, the presence of external fields, the dimensionality of space, etc.

A comprehensive study of coarsening in such model systems is relevant for a wide variety of experimental systems, particularly in block-copolymer systems [4], ferrofluids [5], charged colloidal suspensions [6], ferromagnetic films kept at constant magnetization [7], and Langmuir monolayers [8]. Experiments carried out recently in these last two systems show a very interesting coupling between topological disorder and polydispersity.

In previous work [9–13], we have studied the dynamics of quenched quasi-two-dimensional systems with a scalar order parameter and competing interactions, using a Langevin description. Specifically, we concentrated on the late-stage kinetics for these systems when quenched into the hexagonal phase with cylindrical domains (or disk domains in the two-dimensional case) [12,13]. We studied the mechanisms of defect collision and the growth of order as the system evolves towards a monodisperse state characterized by hexagonal order. We also found a polydisperse regime where the domains coarsen with a reduced growth exponent. In this paper, we take a different approach. We specifically study how the presence of the LRRI affects the classical Ostwald ripening mechanism. Starting from a Ginzburg-Landau free energy description, we derive a set of equations describing both the growth and motion of the minority phase droplets. Recently, we presented a brief discussion of the main results of this approach [14]. This description has some interesting advantages over the Langevin representation: it allows one to decouple the different contributions to the chemical potential that are responsible for different behavior in the system and it consumes far less computer time (and thus one can probe very late times). We find different regimes. In one regime, the "monodisperse hexagonal" regime, the system becomes essentially monodisperse, i.e., the radius distribution function becomes highly peaked on the equilibrium value, and the system seeks the hexagonal order mainly through collision and annihilation of defects. There are also steady-state regimes characterized by polydispersity with a strong coupling between the coordination number of droplets and their size. One of such polydisperse

states is found to be noncoarsening and the system is kinetically frozen. In the other polydisperse state the system coarsens with a radius growth exponent $n < 1/3$. In this paper we extend and describe in detail this work. Section II derives the interfacial equations for model B with LRRI and presents the multidroplet diffusion equation. Section III describes our simulations. Section IV gives the results of the simulations. Finally, Sec. V gives a brief summary.

II. MODEL

A. Interface dynamics for model B with long-range repulsive interactions

The Ginzburg-Landau free energy functional F appropriate for our system is written in dimensionless form as

$$F\{\psi\} = \int d^2r \left[\frac{1}{2}(\nabla\psi)^2 + f(\psi)\right] + \frac{\beta}{2}\int\int d^2r d^2r' \psi(\mathbf{x}) g(|\mathbf{x}-\mathbf{x}'|)\psi(\mathbf{x}'), \quad (1)$$

where β is the strength of the LRRI relative to the *attractive* square gradient term. The order parameter ψ can be written as $\psi = \psi_{\text{off}} + \delta\psi$, where $\delta\psi$ represents the *fluctuations* about zero mean and ψ_{off} is the off-criticality. $F\{\psi\}$ contains both an *attractive* square gradient term and a long-range *repulsive* term whose kernel is $g(|\mathbf{x}-\mathbf{x}'|)$. The local free energy has a double-well structure below the critical temperature. In dimensionless form it is $f(\psi) = -\frac{1}{2}\psi^2 + \frac{1}{4}\psi^4$.

The time evolution of such a system following a quench from the high-temperature disordered phase is given by the appropriate Langevin equation

$$\frac{\partial\psi(\mathbf{x},\tau)}{\partial\tau} = \nabla^2\left[\mu_B(\psi) - \nabla^2\psi + \beta\int d^dx' g(|\mathbf{x}-\mathbf{x}'|)\psi(\mathbf{x}',t)\right], \quad (2)$$

where we neglect noise, and the overall Laplacian takes into account the conservation law associated with the order parameter. The diffusion part of the chemical potential is

$$\mu(\psi) = \mu_B(\psi) - \nabla^2\psi, \quad (3)$$

where $\mu_B(\psi) = \partial f/\partial\psi$ is the bulk chemical potential.

We derive the interfacial equations from the above coarse-grained description using the method of matched asymptotic expansions [15–17]. We use the method of Pego [16], who derived the interfacial equations from the Cahn-Hilliard equation. In order to do that, we need to find how the relevant quantities scale with a quantity l, proportional to the ratio of a macroscopic length—like a typical domain size—to the interfacial width. The diffusive chemical potential $\mu(\psi)$ is proportional to the curvature κ so it scales as $\mu(\psi) \sim l^{-1}$. We consider the long-range term. The kernel we have used previously for our two-dimensional (2D) study is

$$g(|\mathbf{x}-\mathbf{x}'|) = \frac{1}{|\mathbf{x}-\mathbf{x}'|} - \frac{1}{[(\mathbf{x}-\mathbf{x}')^2 + L^2]^{\frac{1}{2}}} \sim \frac{1}{2}\frac{L^2}{|\mathbf{x}-\mathbf{x}'|^3} + \cdots, \quad (4)$$

appropriate for a ferromagnetic film of thickness L or a Langmuir monolayer of thickness L. The right-hand side (rhs) expansion is valid for small values of L. The thickness L is a nonscaling length for the two-dimensional domains, so that to leading order we can consider $g \sim l^{-3}$. In general, we can assume a long-range integral for any dimension such that its kernel satisfies

$$\int d^dx' g(|\mathbf{x}-\mathbf{x}'|)\psi(\mathbf{x}',t) \sim l^{-\eta'}. \quad (5)$$

Since the expression in large square brackets in Eq. (2) is a chemical potential and thus behaves like l^{-1}, then the LRRI coefficient scales with l as $\beta \sim l^{-1+\eta'}$. In our case $\eta' = 1$.

To apply the method of matched asymptotic expansions, we consider $\epsilon \sim l^{-1}$ to be the small expansion parameter. The system is partitioned into bulk (outer) and interfacial (inner) regions. The interfacial region is defined as a skin around the interface Γ of thickness larger than $O(1)$ but less than the macroscopic lengths, which are $O(1/\epsilon)$. The bulk region can be divided in two subregions Ω_- and Ω_+, characterized by negative and positive values of the order parameter and separated by the interface Γ. The order parameter and the chemical potential are expanded in ϵ to the different orders. Differential equations for ψ and μ are obtained for different orders in each region and matched to the same order at the boundary between the regions. For details of the calculation, we refer the reader to the Appendix. Here we quote the resulting equations

$$\nabla^2\left[\mu + \beta\int_\Omega d^dx' g(|\mathbf{x}-\mathbf{x}'|)\psi_0(\mathbf{x}')\right] = 0, \quad (6)$$

$$\mu\big|_\Gamma = -\frac{\kappa(s)\sigma}{\Delta\psi_{\text{eq}}}, \quad (7)$$

$$\Delta\psi_{\text{eq}} v_n = \left[\hat{\mathbf{n}}\cdot\nabla\mu\right]_\Gamma. \quad (8)$$

In these equations $\psi_0(\mathbf{x}) = \psi_{\text{eq}}^+$ in Ω_+, $\psi_0(\mathbf{x}) = \psi_{\text{eq}}^-$ in Ω_-, $\Delta\psi_{\text{eq}} = \psi_{\text{eq}}^+ - \psi_{\text{eq}}^-$, and σ is the surface tension. Equation (6) is the equation describing the bulk dynamics of the order parameter field to first order in ϵ. At this order, the quasistatic approximation $\partial\psi/\partial T = 0$ in the bulk is valid. Equation (7) is the Gibbs-Thompson boundary condition, which arises from a statement of local equilibrium and expresses the fact that the order parameter near a curved interface is determined by the local curvature and the local surface tension. Equation (8) indicates that the normal velocity of the interface is proportional to the discontinuity of the chemical potential across the interface.

B. Multidroplet diffusion equation

We integrate the previous equations formally. Equations (6) and (7) constitute a Dirichlet problem for μ. Once μ is known, Eq. (8) is used to determine the normal velocity v_n. Alternatively, we can write an integral equation for v_n.

Assume a function $\mathcal{F}(\mathbf{x})$ that satisfies the Poisson equation

$$\nabla^2\mathcal{F}(\mathbf{x}) = -a\rho(\mathbf{x}) \ , \tag{9}$$

where $a = 2\pi^{(d/2)}/\Gamma(d/2)$. Let $\mathcal{F}(s)$ and $\partial\mathcal{F}(s)/\partial n$ be the values of this function and of its normal derivative at a point s on a surface Γ. Call $G(\mathbf{x},\mathbf{x}')$ the corresponding Green function that satisfies

$$\nabla^2 G(\mathbf{x},\mathbf{x}') = -a\delta(\mathbf{x}-\mathbf{x}'). \tag{10}$$

We consider the volume Ω_- bounded by the surface Γ, whose unit normal vector is $\hat{\mathbf{n}}$, and the volume Ω_+ bounded by the surface Γ (whose unit normal vector is $-\hat{\mathbf{n}}$) and some surface at infinity. Then the formal solution to the Poisson equation with boundary conditions can be obtained using Green's integral identity in each volume and then applying $\Omega = \Omega_+ + \Omega_-$:

$$\int_\Omega [\mathcal{F}(\mathbf{x}')\nabla^2 G(\mathbf{x},\mathbf{x}') - \nabla^2\mathcal{F}(\mathbf{x}')G(\mathbf{x},\mathbf{x}')]d^dx'$$

$$= h(\tau) + \int_\Gamma G(\mathbf{x},\mathbf{x}(s'))\left[\frac{\partial\mathcal{F}(s')}{\partial n'}\bigg|_+ - \frac{\partial\mathcal{F}(s')}{\partial n'}\bigg|_-\right]ds'$$
$$- \int_\Gamma \frac{\partial G(\mathbf{x},\mathbf{x}(s'))}{\partial n'}[\mathcal{F}(s')|_+ - \mathcal{F}(s')|_-]ds', \tag{11}$$

where $h(\tau)$ is an integration constant. We identify $\mathcal{F}$ with the chemical potential μ. The lhs of Eq. (11) becomes $-a[\mu(\mathbf{x}) + \beta\int_\Omega d^dx' g(|\mathbf{x}-\mathbf{x}'|)\psi_0(\mathbf{x}')]$ while the rhs is given by the interface equations $[\mu(s')|_+ - \mu(s')|_-] = 0$ and $[(\partial\mu(s')/\partial n')|_+ - (\partial\mu(s')/\partial n')|_-] = \Delta\psi_{\rm eq} v_n$. Thus we can write this last equation as

$$\mu(\mathbf{x}) + \beta\int_\Omega d^dx' g(|\mathbf{x}-\mathbf{x}'|)\psi_0(\mathbf{x}')$$

$$= -\frac{\Delta\psi_{\rm eq}}{a}\int_\Gamma ds' G(\mathbf{x},\mathbf{x}(s'))v_n(s') + h(\tau) \ . \tag{12}$$

The integral on the rhs is, in analogy with electrostatics, the potential produced by a surface charge $\sigma(s)$,

$$\sigma(s) = -\frac{\Delta\psi_{\rm eq}}{a}v_n(s). \tag{13}$$

The surface charge $\sigma(s)$ originates in the discontinuity of the normal derivative of μ on the boundary. We use curvilinear coordinates (see the Appendix) and write $\nabla^2 G(s,u;s',u') = -a\delta(s-s')\delta(u-u')$. An equivalent way to write Eq. (12) is

$$\nabla^2\left[\mu(\mathbf{x}) + \beta\int_\Omega d^dx' g(|\mathbf{x}-\mathbf{x}'|)\psi_0(\mathbf{x}')\right] = -a\sigma(s)\delta(u). \tag{14}$$

Now we apply these equations to a set of N spherical droplets characterized by a positive value of the order parameter immersed in a background B characterized by a negative value of the order parameter. Let D_i represent a spherical domain of radius R_i, $D_i = vR_i^d$, and S_i be its surface, $S_i = aR_i^{d-1}$ [with $a = 2\pi^{(d/2)}/\Gamma(d/2)$ and $v = a/d$]. The integral in Eq. (6) can be written as:

$$\frac{1}{\psi_{\rm eq}}\int_\Omega d^dx' g(|\mathbf{x}-\mathbf{x}'|)\psi_0(\mathbf{x}')$$

$$= -\int_B d^dx' g(|\mathbf{x}-\mathbf{x}'|) + \sum_{i=1}^N\int_{D_i} d^dx_i' g(|\mathbf{x}-\mathbf{x}_i'|)$$
$$= -\int_\Omega d^dx' g(|\mathbf{x}-\mathbf{x}'|) + 2\sum_{i=1}^N\int_{D_i} d^dx_i' g(|\mathbf{x}-\mathbf{x}_i'|). \tag{15}$$

The function $g(|\mathbf{x}-\mathbf{x}'|)$ is translationally invariant so that $\int_\Omega d^dx' g(|\mathbf{x}-\mathbf{x}'|)$ is a constant. To first order, μ can be written as $\mu = \chi^{-1}\psi_1$, where χ is the susceptibility defined as $\chi = (\partial\mu/\partial\psi)_{\rm eq}^{-1}$. Our dimensionless coarse-grained double-well energy density gives $\chi^{-1} = 3\psi_{\rm eq}^2 - 1 \simeq 2$. According to our expansion (see the Appendix), $\psi_1(\mathbf{x}) = \psi(\mathbf{x}) - \psi_0(\mathbf{x})$. We define a variable $\theta(\mathbf{x})$

$$\theta(\mathbf{x}) = \frac{\psi(\mathbf{x}) - \psi_0(\mathbf{x})}{\psi_{\rm eq}} \ . \tag{16}$$

The normal coordinate u to a given droplet can be written as $u = R - r$; the curvature is $\kappa = \nabla\cdot\hat{\mathbf{n}} = -(d-1)/R$ and the velocity is $v_n = \partial u/\partial t = \dot{R}$. Equation (7) becomes $\theta(R_i) = [(d-1)\sigma]/(4\psi_{\rm eq}^2 R_i)$.

In the original Langevin problem, distances are rescaled by a characteristic length ξ and time by a characteristic time t^* such that the dimensioned length and time scales are recovered by $\mathbf{r} = \xi\mathbf{x}$ and $t = t^*\tau$. In terms of the free energy parameters l_ϕ (proportional to the interface thickness; the coefficient of the squared gradient in the free energy density is $l_\phi^2/2$) and r (proportional to $|T - T_c|$; the coefficient of the square term in the free energy density is $-r/2$) the characteristic length is given by $\xi = l_\phi/\sqrt{r}$ and the characteristic time is given by $t^* = \xi^2/(rD)$, where D is the mobility in the original Langevin equation [11]. Given the dimensionless quantity L_0,

$$L_0 = \frac{(d-1)\sigma}{4\psi_{\rm eq}^2}, \tag{17}$$

we can define a capillary length l_c and a related time scale, τ_c given by

$$l_c = L_0\xi \ , \tag{18}$$

$$\tau_c = L_0^2 t^* \ . \tag{19}$$

We rescale the coordinates by the quantity L_0 and time by the quantity L_0^2 but keep the same notation, i.e., $\mathbf{x}_{\rm new} = \mathbf{x}_{\rm old}/L_0$ and $\tau_{\rm new} = \tau_{\rm old}/L_0^2$. Equations (6)–(8) become

$$\nabla^2\left[\theta(\mathbf{x}) + \beta\sum_{i=1}^{N}\int_{D_i} d^d x_i' g(|\mathbf{x}-\mathbf{x}_i'|)\right] = 0\ , \tag{20}$$

$$\theta(R_i) = \frac{1}{R_i}\ , \tag{21}$$

$$\dot{R}_i = \left[\hat{\mathbf{r}}\cdot\nabla\theta\right]_{S_i}\ , \tag{22}$$

where β has been rescaled by the appropriate power of L_0.

These equations are very general. Although we have derived them from a Langevin equation that describes spinodal decomposition, the equations are valid for late stages when the droplets are already formed and the process through which they formed is irrelevant. Equally well, they describe the process of Ostwald ripening for droplets formed in the metastable region, once the process of nucleation has stopped. Now we can forget about the Langevin description and take Eqs. (20)–(22) as the fundamental set of equations. Equation (20) is the steady state diffusion equation. Equation (21) is the Gibbs-Thomson boundary condition that states that local equilibrium exists at the particle-matrix interface. Equation (22) is the flux conservation condition at each point of the interface of a droplet.

The generalization of Eq. (12) is straightforward. We assume that the different interfaces are given by a set of curvilinear coordinates $\{u_i, s_i\}$

$$\theta(\mathbf{x}) + \beta\sum_{i=1}^{N}\int_{D_i} d^d x_i' g(|\mathbf{x}-\mathbf{x}_i'|)$$

$$= -\frac{1}{a}\sum_{i=1}^{N}\int_{S_i} ds' G(\mathbf{x},\mathbf{x}(u_i,s'))\dot{R}_i(s') + h(\tau)\ . \tag{23}$$

This equation means that each sphere D_i has a surface charge $\sigma_i(s)$

$$\sigma_i(s) = -\frac{1}{a}\dot{R}_i(s) \tag{24}$$

and the differential form of Eq. (23) is

$$\nabla^2\left[\theta(\mathbf{x}) + \beta\sum_{i=1}^{N}\int_{D_i} d^d x_i' g(|\mathbf{x}-\mathbf{x}_i'|)\right]$$

$$= -a\sum_{i=1}^{N}\sigma_i(s)\delta(u-u_i). \tag{25}$$

This is the multidroplet diffusion equation for systems with LRRI's. It has been known in literature (for systems without LRRI's) in its monopole approximation. Recently, Akaiwa and Voorhees solved the multidroplet diffusion equation without LRRI's using a multipole expansion method [18]. They found that, beyond a certain volume fraction, the monopole approximation does not give a complete description: interparticle diffusional interactions generate distortions of spherical shape that translate into particle migration. However, the LRRI stabilizes the spherical shape and is the main cause of particle motion, so we expect the monopole approximation to be valid for higher volume fractions.

To see how the monopole approximation works, assume a single spherical precipitate. The corresponding δ function is $\delta(\mathbf{x}-\mathbf{R}) = \delta(u-u_1)\delta(s-s_1)$ with

$$\delta(u-u_1) = \delta(r-R)$$

and

$$\delta(s-s_1) = \frac{1}{aR^{d-1}}\delta(\omega-\omega_1). \tag{26}$$

For a single spherical precipitate, the result of applying the Laplacian to the rhs of Eq. (23) gives

$$aR^{d-1}\left[\frac{1}{a}\int\delta(\mathbf{x}-\mathbf{R})\dot{R}(w)dw\right]. \tag{27}$$

The monopole approximation, valid for precipitates that are far apart, consists in replacing the coordinates $\mathbf{R}$ over the surface of the sphere by the coordinates of its center of mass $\mathbf{X}_1$. This means replacing Eq. (27) by

$$aR^{d-1}\dot{R}\delta(\mathbf{x}-\mathbf{X}_1) \tag{28}$$

with

$$\dot{R} = \frac{1}{a}\int\dot{R}(w)dw. \tag{29}$$

Equation (25) becomes

$$\nabla^2\left[\theta(\mathbf{x}) + \beta\sum_{i=1}^{N}\int_{D_i} d^d x_i' g(|\mathbf{x}-\mathbf{x}_i'|)\right]$$

$$= a\sum_{i=1}^{N} R_i^{d-1}\dot{R}_i\delta(\mathbf{x}-\mathbf{X}_i). \tag{30}$$

This is the monopole approximation for the multidroplet diffusion equation for systems with LRRI's in the quasistationary approximation. The local chemical potential is $\mu(\mathbf{x}) = 2\psi_{\rm sat}\Theta(\mathbf{x})$, where $\Theta(\mathbf{x})$ is given by

$$\Theta(\mathbf{x}) = \theta(\mathbf{x}) + \beta\sum_{i=1}^{N}\int_{D_i} d^d x_i' g(|\mathbf{x}-\mathbf{x}_i'|). \tag{31}$$

Obviously $\Theta(\mathbf{x})$ is also function of the set of radii $\{R_i\}$ and the set of coordinates $\{X_i\}$. We write the multidroplet equation as

$$\nabla^2\Theta(\mathbf{x}) = a\sum_{i=1}^{N} B_i\delta(\mathbf{x}-\mathbf{X}_i). \tag{32}$$

Thus B_i is the strength of the source or sink of current for diffusion. On the surface of droplet i, $\Theta(\mathbf{x})$ is

$$\Theta(\mathbf{x})|_{|\mathbf{x}-\mathbf{X}_i|=R_i} = \frac{1}{R_i} + \beta \sum_{j=1}^{N} \int_{D_j} d^d x'_j g(|\mathbf{R}_i - \mathbf{x}'_j|). \tag{33}$$

This is the Gibbs-Thomson boundary condition (notice that the vector $\mathbf{R}_i$ is given by $\mathbf{R}_i = \mathbf{X}_i + R_i \hat{r}$). We can divide the rhs of this equation into three terms. The first term is the LSW contribution to the chemical potential

$$I_{\rm LSW} = \frac{1}{R_i}. \tag{34}$$

The second term is the integral over domain i, which we call the intradomain term. This term is also independent of coordinates and, if distortions from the spherical shape are not allowed, the term only depends on R_i (i.e., has no angular dependence):

$$I_{\rm intra} = \beta \int_{D_i} d^d x'_i g(|\mathbf{R}_i - \mathbf{x}'_i|). \tag{35}$$

The third term gives the interaction of all the other particles with particle i; we call this term the interdomain term and it depends on the positions of all the particles

$$\begin{aligned} I_{\rm inter} &= \beta \sum_{\substack{j=1 \\ j\neq i}}^{N} \int_{D_j} d^d x'_j g(|\mathbf{R}_i - \mathbf{x}'_j|) \\ &\simeq \beta \sum_{\substack{j=1 \\ j\neq i}}^{N} \int_{D_j} d^d x'_j g(|\mathbf{X}_i - \mathbf{x}'_j|), \end{aligned} \tag{36}$$

where the second equality has been obtained by replacing $\mathbf{R}_i$ by the center-of-mass coordinate $\mathbf{X}_i$.

Associated with the rescaled chemical potential $\Theta(\mathbf{x})$ there is a mass flux density

$$\mathbf{j} = -\nabla \Theta(\mathbf{x}) \tag{37}$$

with a purely diffusive term and a term due to the LRRI. The mass balance equation requires

$$\frac{d(vR_i^d)}{d\tau} = -\int_{S_i} \mathbf{j} \cdot \hat{\mathbf{n}}\, dS\ . \tag{38}$$

The evaluation of this flux on the droplet surface S_i gives the growth law

$$R_i^{d-1} \frac{dR_i}{d\tau} = B_i, \tag{39}$$

as before. Conservation of the total flux in the system requires

$$\sum_{i=1}^{N} B_i = 0\ . \tag{40}$$

The above equations describe the growth of the droplets and in the absence of the LRRI, when applied to spherical precipitates, reduce to those of the LSW mechanism with a finite volume fraction. However, in systems with a LRRI these must be augmented by an equation describing the translation of the individual droplets since the droplets assume a specific spatial pattern. We write $D_i = vR_i^d$ and write the change of the center-of-mass coordinate of droplet i as

$$\begin{aligned} &\mathbf{X}_i(\tau + d\tau) - \mathbf{X}_i(\tau) \\ &= \frac{1}{D_i(\tau + d\tau)} \int_{D_i(\tau + d\tau)} d^d x\ \mathbf{x}\ \frac{\psi(\mathbf{x}, \tau + d\tau)}{\psi_{\rm eq}} \\ &\quad - \frac{1}{D_i(\tau)} \int_{D_i(\tau)} d^d x\ \mathbf{x}\ \frac{\psi(\mathbf{x}, \tau)}{\psi_{\rm eq}}. \end{aligned} \tag{41}$$

Taking the limit $d\tau \to 0$,

$$\begin{aligned} \frac{d\mathbf{X}_i}{d\tau} &= \frac{1}{D_i(\tau)} \int_{D_i} d^d x\ \mathbf{x} \frac{1}{\psi_{\rm eq}} \frac{d\psi(\mathbf{x}, \tau)}{d\tau} \\ &= \frac{1}{D_i(\tau)} \int_{S_i} ds\ \mathbf{x}(s) \dot{R}_i(s)\ . \end{aligned} \tag{42}$$

We multiply Eq. (25) by $\mathbf{x}$ and integrate it in the neighborhood of droplet i, i.e., in a volume $\mathcal{D}_i = D_i + \delta D_i$ of radius $R_i + \delta R_i$ (no other droplet touches the volume $\mathcal{D}_i$). Then the above equation turns into

$$D_i(\tau) \frac{d\mathbf{X}_i}{d\tau} = \int_{\mathcal{D}_i} d^d x\ \mathbf{x}\ \nabla^2 \Theta(\mathbf{x})\ . \tag{43}$$

The rhs of this equation can be written as

$$\sum_{\alpha=1}^{d} \hat{\mathbf{x}}_\alpha \int_{\mathcal{D}_i} d^d x\ \nabla \cdot (x_\alpha \nabla \Theta) - \int_{\mathcal{D}_i} d^d x \nabla \Theta\ , \tag{44}$$

where α refers to the components of vector $\mathbf{x}$. The essential mechanism for the motion of the droplet is diffusion along the droplet interface of particles belonging to the droplet itself. The droplet moves deforming only slightly, without changing its volume. By using the monopole approximation and considerations of symmetry, it can be shown that neither $I_{\rm LSW}$ nor $I_{\rm intra}$ contributes to Eq. (44). Thus we are left with the interdomain term. Since this integral is continuous at the interface, we can take the limit $\delta D_i \to 0$ or $\mathcal{D}_i \to D_i$. The direct evaluation of the second term in Eq. (44) gives $-\beta \sum_{j\neq i} \int_{D_i} d^d x_i \int_{D_j} d^d x'_j \nabla_i g(|\mathbf{x}_i - \mathbf{x}'_j|)$. We write $\mathbf{x}_i = \mathbf{X}_i + \mathbf{r}_i$, where $\mathbf{r}_i$ is a vector that originates in the center of mass of the droplet. Thus we can write $\int_{D_i} d^d x_i \int_{D_j} d^d x'_j \nabla_i g(|\mathbf{x}_i - \mathbf{x}'_j|) \equiv \nabla_{\mathbf{X}_i} \int_{D_i} d^d r_i \int_{D_j} d^d r'_j g(|\mathbf{X}_{ij} + \mathbf{r}_i - \mathbf{r}'_j|)$, where $\mathbf{X}_{ij} = \mathbf{X}_i - \mathbf{X}_j$. The evaluation of the first term requires some algebra. In the monopole approximation this term gives $-\beta v R_i^d \sum_{j\neq i} v R_j^d [\partial g(X_{ij})/\partial X_{ij}] \hat{X}_{ij}$, with $\hat{X}_{ij} = \mathbf{X}_{ij}/X_{ij}$. Thus, within the monopole approximation, the equation of motion can be written as

$$\begin{aligned} \frac{d\mathbf{X}_i}{d\tau} = -\frac{2\beta}{vR_i^d} \sum_{\substack{j=1 \\ j\neq i}}^{N} \nabla_{\mathbf{X}_i} \int_{D_i} d^d r_i \int_{D_j} d^d r'_j \\ \times g(|\mathbf{X}_{ij} + \mathbf{r}_i - \mathbf{r}'_j|)\ . \end{aligned} \tag{45}$$

The interpretation of Eq. (45) is straightforward. The interaction energy between domains i and j is U_{ij}:

$$U_{ij} = \beta \int_{D_i} d^d r_i \int_{D_j} d^d r'_j g(|\mathbf{X}_{ij} + \mathbf{r}_i - \mathbf{r}'_j|) \tag{46}$$

and Eq. (45) can be written as

$$\frac{d\mathbf{X}_i}{d\tau} = -\frac{M}{v R_i^d} \sum_{j \neq i} \nabla_{\mathbf{X}_i} U_{ij}. \tag{47}$$

This means that the motion of center-of-mass coordinates is described by a Langevin equation with mobility inversely proportional to the volume of the droplet. A numerical factor M sets the relative time scale of the hexagonal ordering of the droplets to the LSW mechanism. The motion is given by the interdomain contribution, i.e., the positioning of surrounding droplets, mediated through the LRRI. We treat M as a phenomenological parameter in order to study the effects of enhancing or hindering hexagonal order and to allow for different modes of mass transport for different LRRI systems.

III. SIMULATIONS

The set of equations formed by the diffusion equation Eq. (32), the Gibbs-Thomson boundary condition Eq. (33), the growth law Eq. (39), the conservation law Eq. (40), and the motion of coordinates Eq. (47) constitute a formal solution of the LSW problem for systems with LRRI's. The advantage of this approach is that, unlike the Langevin formulation, all the factors contributing to the LSW mechanism and the LRRI may be decoupled and studied directly. To solve these equations, a generalization of the numerical technique previously described in the literature [19] was used.

The solution of Eq. (32) in two dimensions is

$$\Theta(\mathbf{x}) = B_0 + \sum_{i=1}^{N} B_i \ln|\mathbf{x} - \mathbf{X}_i| \ , \tag{48}$$

where B_0 is an integration constant. The Gibbs-Thomson boundary condition reads

$$\begin{aligned} \Theta(\mathbf{x})|_{|\mathbf{x}-\mathbf{X}_i|=R_i} &= \frac{1}{R_i} + \beta \sum_{j=1}^{N} \int_{D_j} d^d x'_j g(|\mathbf{R}_i - \mathbf{x}'_j|) \\ &= B_0 + B_i \ln|\mathbf{R}_i - \mathbf{X}_i| + \sum_{\substack{j=1 \\ j\neq i}}^{N} B_j \ln|\mathbf{R}_i - \mathbf{X}_j|, \end{aligned} \tag{49}$$

which can be written as

$$\Theta(R_i) = B_0 + B_i \ln R_i + \sum_{\substack{j=1 \\ j\neq i}}^{N} B_j \ln\Big(|\mathbf{X}_i - \mathbf{X}_j|^2 + R_i^2 - 2R_i|\mathbf{X}_i - \mathbf{X}_j|\cos\gamma_{ij}\Big)^{1/2}, \tag{50}$$

where γ_{ij} is the angle between vectors $\mathbf{R}_i - \mathbf{X}_i$ and $\mathbf{X}_i - \mathbf{X}_j$. The monopole approximation consists of averaging over the angle γ_{ij}. In this approximation the Gibbs-Thomson boundary condition becomes

$$\Theta(R_i) = B_0 + B_i \ln R_i + \sum_{\substack{j=1 \\ j\neq i}}^{N} B_j \ln|\mathbf{X}_j - \mathbf{X}_i|. \tag{51}$$

To provide equations suitable for numerical simulations, we follow Yao *et al.* [19]. We split Θ in two pieces, i.e., $\Theta = \Theta_1 + \Theta_2$, which are solutions of the equations

$$\nabla^2 \Theta_1 = -2\pi\rho_1(\mathbf{x}) \tag{52}$$

and

$$\nabla^2 \Theta_2 = -2\pi\rho_2(\mathbf{x}) \ , \tag{53}$$

where

$$\rho_1(\mathbf{x}) = -\frac{\eta}{\pi} \sum_{j=1}^{N} B_j \ \exp\left[-\eta|\mathbf{x} - \mathbf{X}_j|^2\right], \tag{54}$$

$$\rho_2(\mathbf{x}) = \frac{\eta}{\pi} \sum_{j=1}^{N} B_j \ \exp\left[-\eta|\mathbf{x} - \mathbf{X}_j|^2\right] - \sum_{j=1}^{N} B_j \delta(\mathbf{x} - \mathbf{X}_j) \tag{55}$$

and η is a positive constant. The solution of Eq. (52) is

$$\Theta_1(\mathbf{x}) = -\frac{1}{2\pi} \sum_{j=1}^{N} B_j \int \frac{e^{-\frac{k^2}{4\eta}}}{k^2} e^{i\mathbf{k}\cdot(\mathbf{x}-\mathbf{X}_j)} d\mathbf{k} \tag{56}$$

and that of Eq. (53) is

$$\Theta_2(\mathbf{x}) = \sum_{j=1}^{N} B_j \ln|\mathbf{x} - \mathbf{X}_j| - \frac{\eta}{\pi} \sum_{j=1}^{N} B_j \int \ln|\mathbf{x} - \mathbf{x}'| e^{-\eta|\mathbf{x}' - \mathbf{X}_j|^2} d\mathbf{x}', \tag{57}$$

which can be reduced to

$$\Theta_2(\mathbf{x}) = -\sum_{j=1}^{N} B_j \int_{|\mathbf{x}-\mathbf{X}_j|}^{\infty} \frac{e^{-\eta x'^2}}{x'} dx'. \tag{58}$$

Combining these expressions we get

$$\Theta(\mathbf{x}) = B_0 - \frac{1}{2\pi} \sum_{j=1}^{N} B_j \int \frac{e^{-\frac{k^2}{4\eta}}}{k^2} e^{i\mathbf{k}\cdot(\mathbf{x}-\mathbf{X}_j)} d\mathbf{k} - \sum_{j=1}^{N} B_j \int_{|\mathbf{x}-\mathbf{X}_j|}^{\infty} \frac{e^{-\eta x'^2}}{x'} dx'. \tag{59}$$

Yao *et al.* found a tractable form of Eq. (51), which we express here in rescaled quantities. If L_B represents the system size, we can rescale radii, coordinates, and the coefficients B_i as $R_i \equiv R_i/L_B$, $X_i \equiv X_i/L_B$, and $B_i \equiv B_i L_B$. We identify the rescaled quantities with the same notation as the unrescaled ones to avoid introducing a new notation. Notice that time rescales as $\tau \equiv \tau/L_B^3$. We also set $\eta = 1/L_B^2$. The final form for Eq. (51) in the rescaled quantities is

$$\frac{1}{R_i} + \beta L_B^2 \sum_{j=1}^{N} \int_{D_j} d^d x'_j g(|\mathbf{R}_i - \mathbf{x}'_j|)$$

$$= B_0 + B_i \left[\ln R_i + \int_0^1 \frac{1 - e^{-x'^2}}{x'} dx' - \int_1^\infty \frac{e^{-x'^2}}{x'} dx' \right]$$

$$- \sum_{\substack{j=1 \\ j \neq i}}^{N} B_j \int_{|\mathbf{x}-\mathbf{X}_j|}^{\infty} \frac{e^{-x'^2}}{x'} dx'$$

$$-2\pi \sum_{j=1}^{N} B_j \sum_{\mathbf{k} \neq \mathbf{0}} \frac{e^{-\frac{k^2}{4}}}{k^2} e^{i\mathbf{k}\cdot(\mathbf{X}_j - \mathbf{X}_i)}. \tag{60}$$

The apparent singularity in the last term at $\mathbf{k} = \mathbf{0}$ is eliminated due to Eq. (40).

Now we have to deal with the lhs of Eq. (60), i.e., with the long-range term. As stated in Eqs. (35) and (36), the long-range term can be divided in an intradomain term, independent of coordinates, and an interdomain term, which depends on the positions of all particles. Here we write explicitly the expression of these terms for our specific 2D kernel given by Eq. (4) for a film of thickness L. For the intradomain term we write $\mathbf{x}' = \mathbf{X} + \mathbf{r}'$, where $\mathbf{r}'$ is the radial coordinate from the center of mass $\mathbf{X}$ of the droplet. This term becomes

$$\beta^{-1} I_{\text{intra}} = \int_0^R dr'\, r' \int_0^{2\pi} d\phi' \{ [R^2 + r'^2 - 2Rr' \cos(\phi - \phi')]^{-\frac{1}{2}} - [R^2 + L^2 + r'^2 - 2Rr' \cos(\phi - \phi')]^{-\frac{1}{2}} \}$$

$$= 2R \int_0^1 dp\, p I(p, l)\ , \tag{61}$$

where $\phi - \phi'$ is the angle between the vectors $\mathbf{R} - \mathbf{X}$ and $\mathbf{r}'$, $p = r'/R$, $l = L/R$, and $I(p,l)$ is given by

$$I(p,l) = \int_0^\pi d(\Delta\phi) \left[\left(1 + p^2 - 2p\cos\Delta\phi\right)^{-\frac{1}{2}} - \left(1 + l^2 + p^2 - 2p\cos\Delta\phi\right)^{-\frac{1}{2}} \right]. \tag{62}$$

Consider the second term in the above expression. Taking into account that $\int_0^\pi d\phi (1 + l^2 + p^2 \pm 2p\cos\phi)^{-\frac{1}{2}}$ has the same value independent of the sign in front of the cosine term, we can write

$$\int_0^\pi d\phi \left(1 + l^2 + p^2 - 2p\cos\phi\right)^{-\frac{1}{2}}$$

$$= \frac{2}{\sqrt{(1+p)^2 + l^2}} \int_0^{\frac{\pi}{2}} d(\phi/2) \left(1 - k^2 \sin^2 \frac{\phi}{2}\right)^{-\frac{1}{2}}$$

$$= \frac{2}{\sqrt{(1+p)^2 + l^2}} \mathbf{K}\left(\frac{2\sqrt{p}}{\sqrt{(1+p)^2 + l^2}} \right), \tag{63}$$

where $k^2 = 4p/\left[(1+p)^2 + l^2\right]$ and $\mathbf{K}$ is the complete elliptical integral of the first kind [20]. Taking into account that $\mathbf{K}(2\sqrt{p}/(1+p))/(1+p) = \mathbf{K}(p)$ we can write

$$I_{\text{intra}} = 4\beta R \int_0^1 dp\, p \left[\mathbf{K}(p) - \frac{1}{\sqrt{(1+p)^2 + l^2}} \times \mathbf{K}\left(\frac{2\sqrt{p}}{\sqrt{(1+p)^2 + l^2}} \right) \right]. \tag{64}$$

The interdomain term in Eq. (36) can be written as

$$I_{\text{inter}} = \beta \sum_{\substack{j=1 \\ j \neq i}}^{N} \int_{D_j} d^d x'_j g(|\mathbf{X}_i - \mathbf{x}'_j|)$$

$$= \beta \sum_{\substack{j=1 \\ j \neq i}}^{N} \int_0^{R_j} dr'\, r' \int_0^{2\pi} d\phi_{ij} \left[\left(X_{ij}^2 + r'^2 - 2X_{ij} r' \cos\phi_{ij}\right)^{-\frac{1}{2}} - \left(X_{ij}^2 + L^2 + r'^2 - 2X_{ij} r' \cos\phi_{ij}\right)^{-\frac{1}{2}} \right]$$

$$= \beta \sum_{\substack{j=1 \\ j \neq i}}^{N} 4X_{ij} \int_0^{P_{j,i}} dp\, p \left[\mathbf{K}(p) - \frac{1}{\sqrt{(1+p)^2 + l_{ij}^2}} \mathbf{K}\left(\frac{2\sqrt{p}}{\sqrt{(1+p)^2 + l_{ij}^2}} \right) \right], \tag{65}$$

where $X_{ij} = |\mathbf{X}_i - \mathbf{X}_j|$, $P_{j,i} = R_j/X_{ij}$, $l_{ij} = L/X_{ij}$, and ϕ_{ij} is the angle between $\mathbf{X}_i - \mathbf{X}_j$ and $\mathbf{r}'$. If the domains are far apart, we can also write

$$I_{\text{inter}} = \beta \sum_{\substack{j=1 \\ j \neq i}}^{N} \pi R_j^2 \left[\frac{1}{X_{ij}} - \frac{1}{\left(X_{ij}^2 + L^2\right)^{\frac{1}{2}}} \right]. \tag{66}$$

Our simulations were performed as follows. The system was initialized by generating a set of radii $\{R_i\}$ and a set of centers of mass $\{\mathbf{X}_i\}$ without droplet overlap. In most cases these sets were chosen at random, although we also tried particular configurations, such as initial equal radius configurations or initial hexagonal distributions of coordinates (triangular lattice). Once the initial distri-

butions were chosen, the set of $N+1$ equations formed by Eqs. (60) [with Eqs. (64) and (65)] and (40) were solved to obtain the N values for $\{B_i\}$ and the value for B_0. Then Eqs. (39) and (47) were integrated numerically using a Euler discretization scheme with a small time increment. This generated a new set of radii $\{R_i\}$ and coordinates $\{\mathbf{X}_i\}$ and the process was iterated. We followed the same method of Yao *et al.* [19] to keep the volume fraction constant: the time increment was determined self-consistently by shrinking, at most, one droplet in each single time step. We extended the summations in Eq. (60) to all droplets in the system. Generally, our simulations began with $N_0 = 500$ droplets, distributed either at random or in a triangular lattice in a rectangular box, which requires an equilibrium number of droplets $N_{eq} \leq N_0$. We varied the film thickness $0.1 \leq L \leq 10$ and for each L we tried different values of β, for volume fractions $0.04 \leq \phi_0 \leq 0.40$. The parameter M, which sets the relative time scale of the hexagonal ordering of the droplets to the LSW mechanism, was also varied. During the simulation, the average radius and droplet distribution function were computed. The evolution of the spatial distribution of the droplets and the processes of topological defect annihilation were studied and analyzed using standard Voronoi construction techniques. Selected runs and their corresponding parameters are given in Tables I–IV.

IV. RESULTS

First, we show the effects on the growth rates of the contributions to the chemical potential of the LSW term $I_{\rm LSW}$ [Eq. (34)], the LRRI intradomain term $I_{\rm intra}$ [Eq. (35)], and the LRRI interdomain term $I_{\rm inter}$ [Eq. (36)]. We call the resulting growth rates $V_{\rm LSW}$, $V_{\rm intra}$, and $V_{\rm inter}$, respectively, such that the total growth rate is given by $V_T = \dot{R} = V_{\rm LSW} + V_{\rm intra} + V_{\rm inter}$.

Figures 1 and 2 show the effects of both the spatial and the size distribution of the droplets on the coarsening rates $V_{\rm LSW}, V_{\rm intra}, V_{\rm inter}$, and V_T. Both $V_{\rm LSW}$ and $V_{\rm intra}$ are independent of coordinates while $V_{\rm inter}$ depends crucially on them. Consider a broad radius distribution. $V_{\rm LSW}$ (thin solid line) describes the classical situation in the absence of any LRRI ($\beta = 0$), i.e., droplets with radii smaller than the mean radius R_m have negative growth rates and shrink, while droplets with $R > R_m$ grow. $V_{\rm intra}$ (dashed line) has the opposite behavior: droplets with $R < R_m$ have positive growth rates, while those with $R > R_m$ have negative rates; this term favors a monodisperse droplet distribution. If the radii are chosen uncorrelated (Fig. 1), $V_{\rm inter}$ produces a disperse cloud of points; the dispersion of this distribution increases with volume fraction or with randomness of coordinates. Individual droplet points in the uncorrelated $V_{\rm inter}$ distribution may have any growth rate, depending on their immediate environment. On the other hand, for a strongly correlated system [Fig. 2(b), for example], $V_{\rm inter}$ produces a well defined curve. In both cases, the *average* $V_{\rm inter}$ (dots), like $V_{\rm LSW}$, gives a mass flux from smaller to larger particles, although the slope of this curve can be smaller or larger than that of the $V_{\rm LSW}$ curve.

Figure 1 shows distributions for a film thickness $L = 10$, a volume fraction $\phi_0 = 0.04$, and a random distribution of radii. These figures correspond to the case where the intradomain contribution outweighs the sum of the LSW and the interdomain contributions $|V_{\rm intra}(R)| > |V_{\rm LSW}(R) + V_{\rm inter}(R)|$ such that the total mass flux drives the system to a monodisperse distribution. Figures 1(a)–1(c) correspond to $\beta = 0.36$ and Figs. 1(d)–1(f) correspond to $\beta = 0.08$. For higher β the different contributions V_R of the growth rate have a larger amplitude. In particular, the total growth rate V_T has larger amplitude in systems with higher dipolar strength: these systems reach the monodisperse state sooner than those with lower dipolar strength. Figures 1(a), 1(b), 1(d), and 1(e) show the V_R's for coordinates that correspond to a triangular lattice while Figs. 1(c) and 1(f) show V_T for randomly chosen coordinates. In Figs. 1(a) and 1(d) the thin solid line represents $V_{\rm LSW}$, the dashed line

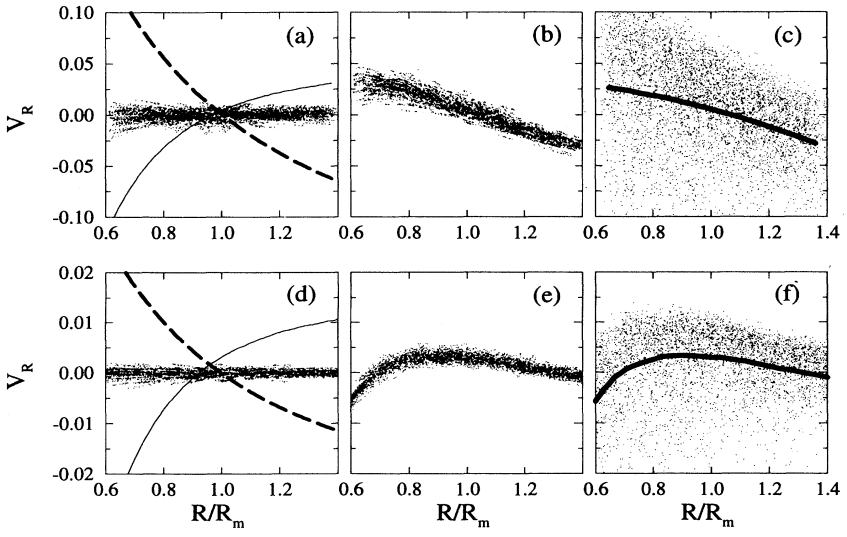

FIG. 1. Growth-rate distributions V_R for $L = 10$, $\phi_0 = 0.04$ and a random radius distribution. Thin solid line, $V_{\rm LSW}$; dashed line, $V_{\rm intra}$. The cloud of points in (a) and (d) represents $V_{\rm inter}$ whereas in (b), (c), (e), and (f), it represents V_T. For (a)–(c), $\beta = 0.36$. For (d)–(f), $\beta = 0.08$. (a), (b), (d), and (e) show V_R for triangular coordinates. (c) and (f) show V_T for random coordinates (the solid line is its average).

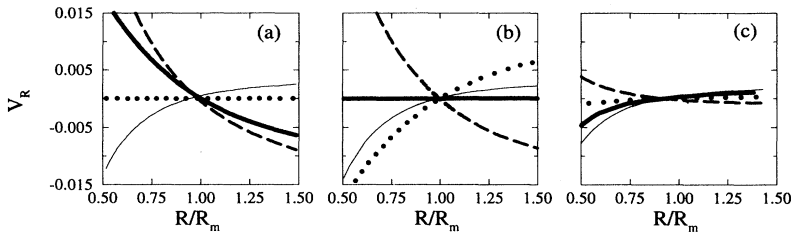

FIG. 2. Growth-rate distributions V_R for $\beta = 0.08$ and $\phi_0 = 0.40$. Thin solid line, $V_{\rm LSW}$; dashed line, $V_{\rm intra}$; dots, $V_{\rm inter}$; thick solid line, V_T. In (a) the average $V_{\rm inter}$ and the *average* V_T are shown. (a) $L = 10$, triangular coordinate distribution and random radii. (b) $L = 10$, distribution corresponding to the frozen state shown in Fig. 5 (run PF4). (c) $L = 2.5$, distribution corresponding to the coarsening state shown in Fig. 6 (run PC4).

represents $V_{\rm intra}$, and the cloud of dots is $V_{\rm inter}$. The total contribution $V_T = V_{\rm LSW} + V_{\rm intra} + V_{\rm inter}$ is shown in Figs. 1(b) and 1(e), respectively. For randomly chosen coordinates $V_{\rm LSW}$ and $V_{\rm intra}$ are the same as for triangular coordinates (they do not depend on coordinates) but $V_{\rm inter}$ and thus V_T are much more disperse, as shown in Figs. 1(c) and 1(f). In these panels the average V_T is indicated with a solid line and essentially is the same as the average V_T for triangular coordinates. For triangular coordinates (and any volume fraction) the average $V_{\rm inter}$ is nearly zero. For coordinates that do not correspond to a triangular lattice, the average $V_{\rm inter}$ gets a positive slope that increases with volume fraction.

In the balance among $V_{\rm LSW}$, $V_{\rm intra}$, and $V_{\rm inter}$ three situations can happen. When $|V_{\rm intra}(R)| > |V_{\rm LSW}(R) + V_{\rm inter}(R)|$ [Figs. 1 and 2(a)], the resulting V_T leads the system to a monodisperse distribution. When $V_{\rm intra}(R) = -(V_{\rm LSW}(R) + V_{\rm inter}(R))$ [Fig. 2(b)], the total growth rate is $V_T = 0$. When $|V_{\rm intra}(R)| < |V_{\rm LSW}(R) + V_{\rm inter}(R)|$ [Fig. 2(c)], the system tends to a polydisperse distribution. Figure 2 shows these three cases for a volume fraction $\phi_0 = 0.40$ and $\beta = 0.08$. Figure 2(a) corresponds to a film thickness $L = 10$, a triangular coordinate distribution, and random radii. A system that starts with such distribution will be driven to a monodisperse state. Figure 2(b) corresponds to a film thickness $L = 10$. This distribution corresponds to the frozen state shown in Fig. 5 (run PF4). Figure 2(c) corresponds to a film thickness $L = 2.5$ and the coarsening state shown in Fig. 6 (run PC4). In the particular case where all the droplets at some instant have equal radii, one has $V_{\rm LSW} = V_{\rm intra} = 0$ and only $V_{\rm inter}$ contributes to V_T. This distribution (not shown) is a set of dots on $R/R_m = 1$ that extends from $V_{\rm min} < 0$ to $V_{\rm max} > 0$. The droplet distribution function is an initial δ function that spreads out as time evolves and the different droplets in the distribution increase or decrease their radii according to their relative positions. This spreading of the radius distribution then brings into play $V_{\rm LSW}$ and $V_{\rm intra}$ and the final state again depends on the balance of the three contributions to V_T. The tendency of $V_{\rm intra}$ to produce a monodisperse distribution and of $V_{\rm inter}$ to produce a strong coupling between the position and size of droplets are features absent in the classical LSW mechanism.

In Eq. (33), $\Theta(R_i)$ can be identified with the energy per unit area of droplet i. To find the equilibrium radius, we have to minimize $\Theta(R)$ with respect to R. First we consider the LSW and the intradomain terms, which for our particular kernel give

$$I_{\rm LSW} + I_{\rm intra} = \frac{1}{R} + 4\beta R \int_0^1 pdp \left[\mathbf{K}(p) - \frac{1}{\sqrt{(1+p)^2 + l^2}} \times \mathbf{K}\left(\frac{2\sqrt{p}}{\sqrt{(1+p)^2 + l^2}} \right) \right], \tag{67}$$

where $l = L/R$. Minimization of this equation gives

$$\frac{1}{R^2} = 4\beta Z(l) - 4\beta l^2 W(l), \tag{68}$$

where the functions Z and W are given by

$$Z(l) = \int_0^1 pdp \left[\mathbf{K}(p) - \frac{1}{\sqrt{(1+p)^2 + l^2}} \times \mathbf{K}\left(\frac{2\sqrt{p}}{\sqrt{(1+p)^2 + l^2}} \right) \right] \tag{69}$$

and

$$W(l) = \int_0^1 \frac{pdp}{\sqrt{(1+p)^2 + l^2}\left[(1-p)^2 + l^2\right]} \times \mathbf{E}\left(\frac{2\sqrt{p}}{\sqrt{(1+p)^2 + l^2}} \right). \tag{70}$$

Here $\mathbf{K}$ and $\mathbf{E}$ are the complete elliptical integrals of the first and the second kind, respectively [20]. The solution of Eq. (68) gives a "bare" equilibrium radius $R = R^0_{\rm eq}$, independent of volume fraction. The interaction term is more difficult to compute. For small values of βL^2 we can take the dipole limit of Eq. (4). In monolayers with a dipolar interaction, the bond number is defined as $N_B = (\Delta p)^2/\sigma$, where Δp is the dipolar density and σ the surface tension. In the limit of thin films, it can be expressed in terms of our parameters as $N_B \equiv \beta L^2/2$. The interaction term for a perfect triangular lattice and dipolar interactions has been computed by McConnell [21]. He finds that the interaction energy per unit area can be expressed as $I_{\rm inter} = N_B G(\phi_0)/R$, where $G(\phi_0)$ is a monotonically increasing function of the volume fraction ϕ_0 and $G(0) = 0$. Thus, if we consider the dipolar

approximation for the interaction term, the minimization of the energy per unit area gives

$$\frac{1+N_B G(\phi_0)}{R^2} = 4\beta Z(l) - 4\beta l^2 W(l), \qquad (71)$$

whose solution is $R = R_{eq}$. Notice that in this approximation the equation for the "complete" equilibrium radius R_{eq}, Eq. (71), is the same as the equation for the bare equilibrium radius R^0_{eq}, Eq. (68), but with a renormalized surface tension $\sigma(\phi_0) = 1 + N_B G(\phi_0)$, which is a monotonically increasing function of ϕ_0 and satisfies $\sigma(0) = 1$. When solving Eq. (71), we have found that there is a value of β_0 for a given film thickness L_0 such that for $\beta < \beta_0$ the only solution is $R_{eq} = \infty$. Figure 3 shows the corresponding phase diagram. The values β_0, L_0, which separate the finite solution from the solution $R_{eq} = \infty$, satisfy $\beta_0 L_0^2 \simeq 0.98\sigma(\phi_0)$. Thus, for $\beta_0 L_0^2 > 0.98\sigma(\phi_0)$ there is a noncoarsening solution with a finite R_{eq}, while $\beta_0 L_0^2 < 0.98\sigma(\phi_0)$ corresponds to the coarsening solution with $R_{eq} = \infty$. The existence of coarsening and noncoarsening solutions depends crucially on the model or on the very specific interactions particular to the real system. However, this phase diagram gives a qualitative idea of what could happen in real experimental systems. Thus the polydisperse coarsening behavior in a two-dimensional binary mixture, reported by Seul *et al.* [8], could have a noncoarsening solution or could have such a large R_{eq} that the noncoarsening behavior cannot be achieved during experimental times. Our model predicts coarsening behavior for bond numbers $N_B < 0.49$.

A. Noncoarsening behavior

Now we present results for those systems that have a finite R_{eq}. Within these, two regimes are found: a monodisperse hexagonal regime and a polydisperse frozen regime. If the system is free to reach hexagonal order then $|V_{intra}| > |V_{LSW} + V_{inter}|$ and the resulting V_T [Figs. 1(b) and 2(a)] leads the system to a monodisperse distribution. This behavior occurs for any mobility $M \geq 0.01$. However, if the hexagonal order is hindered, for instance by taking the limit $M \to 0$, then $V_{intra} = -(V_{LSW} + V_{inter})$ as in Fig. 2(b). The system becomes kinetically frozen in a polydisperse configuration.

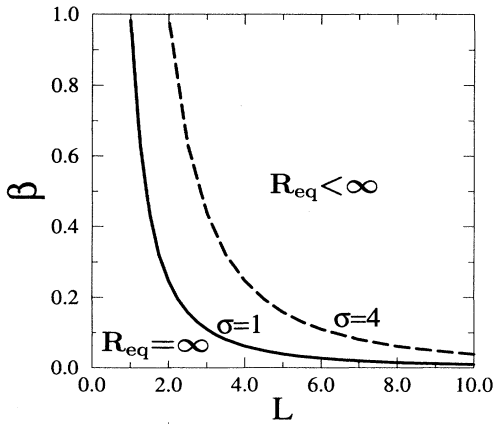

FIG. 3. Phase diagram indicating the regions of coarsening ($R_{eq} = \infty$) and noncoarsening behavior. The solid line corresponds to the "bare" equilibrium radius R^0_{eq} [i.e., with surface tension $\sigma(0) = 1$] and the dashed line corresponds to the equilibrium radius R_{eq} corresponding to a nonzero volume fraction [with renormalized surface tension $\sigma(\phi_0) = 4$].

1. *Monodisperse hexagonal regime*

Table I gives different parameters used to test the monodisperse hexagonal (MH) regime. Figure 4 shows typical configurations for runs MH1 and MH3, i.e., $L = 10$, $\beta = 0.36$, $M = 1$, and $\phi_0 = 0.04$ for MH1 and $\phi_0 = 0.40$ for MH3. Configurations for lower β are qualitatively the same, with fewer droplets. The top panels show the initial configurations (both coordinates and radii random). In both cases, the initial growth-rate distribution is such that the total V_T leads the system to a monodisperse distribution; the initial growth-rate distribution for $\phi_0 = 0.04$ is depicted in Fig. 1(c). The final configurations correspond to a state with equal radii and triangular coordinates, except for a few dislocations. In some runs, the formation of grain boundaries that disrupt the hexagonal order is also observed. The mechanisms of defect annihilation and collision are the same as described in a Langevin simulation study [12,13]. The droplet distribution function evolves from a completely uniform distribution at $\tau = 0$ with $0.5 \leq R/R_m \leq 1.5$ (R_m is the mean radius) to the δ function shown in Fig. 7.

In systems that evolve to a hexagonal state, the magnitude of the hexagonal order present in the early stages stabilizes them against the LSW mechanism [22]. Consider a random radius distribution. For triangular coordinates and not too high volume fractions V_{inter} is a narrow band around $V_R = 0$ so that V_T is positive for $R < R_m$ and negative for $R > R_m$ [Fig. 1(b)]. For random coordinates, V_{inter} is very disperse and although its average behaves as the one for triangular coordinates, many small droplets in the cloud have very negative V_T and are bound to disappear [Fig. 1(c)]. First, we simulated a system with an initial triangular configuration and random radii, run MH5 (Table II). In the final state

TABLE I. Monodisperse hexagonal (MH) regime. L is the film thickness, β is the LRRI strength, ϕ_0 is the volume fraction, M is the mobility parameter. τ_{max} is the maximum time achieved in the simulation, and n_{run} is the number of independent quenches.

Run	L	β	ϕ_0	M	τ_{max}	n_{run}
MH1	10	0.36	0.04	1	176000	20
MH1b	10	0.36	0.04	10	42000	20
MH2	10	0.08	0.04	1	265000	6
MH3	10	0.36	0.40	1	90000	5
MH4	10	0.08	0.40	1	320000	4

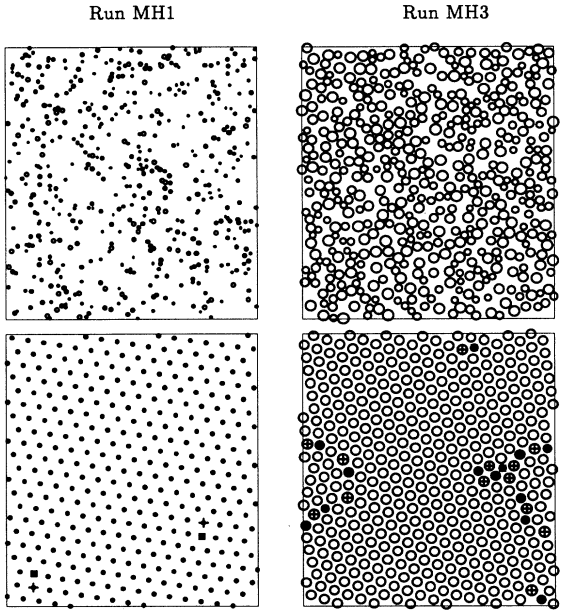

FIG. 4. Configurations for runs MH1 and MH3: $L = 10$, $\beta = 0.36$, and $M = 1$; $\phi_0 = 0.04$ for MH1 and $\phi_0 = 0.40$ for MH3. The top panels correspond to $\tau = 0$ and lower panels to $\tau = 176\,000$ and $\tau = 89\,000$, respectively. The filled symbols correspond to coordination number $z = 5$ and the plus sign to $z = 7$.

the radius distribution is a δ function and the number of droplets is equal to the initial one. Second, the process is repeated with exactly the same parameters and radius distribution but with a random initial distribution of coordinates, run MH6. In this case, the system eliminates several droplets before the radius distribution becomes a δ function. In both cases, the system ends in a triangular configuration, but in the first case the resulting lattice constant is smaller. Keeping everything the same, but varying M, we find similar results. Larger M achieves the hexagonal order faster than smaller M so that systems with higher M are stabilized sooner against the LSW mechanism and therefore their final number of droplets is higher. Runs MH1 and MH1b only differ in the value of the mobility parameter; the initial conditions are exactly the same. At $\tau \sim 400$ each individual run in MH1b reaches a number of droplets that stays constant up to the time where the simulation has finished ($\tau \sim 42\,000$), when the system is a triangular lattice with some dislocations. Finally, we consider run MH7. This run starts with random coordinates but with all radii equal to the equilibrium value. As stated before, in the particular case where all the droplets have equal radii, $V_{\rm LSW} = V_{\rm intra} = 0$; only $V_{\rm inter}$ contributes to V_T. The distribution is a set of dots on $R/R_m = 1$ that extends from $V_{\rm min} < 0$ to $V_{\rm max} > 0$. The droplet distribution function is an initial δ function that spreads out as time evolves and the different droplets in the distribution increase or decrease their radii according to their relative positions. After many droplets disappear the system starts organizing itself in a triangular configuration and the droplet distribution function becomes again a δ function.

2. *Polydisperse frozen regime*

Table III gives different parameters used to test the polydisperse frozen (PF) regime. Figure 5 shows typical configurations for runs PF2 and PF4, i.e., $L = 10$, $\beta = 0.08$, $M = 0.001$, and $\phi_0 = 0.04$ for PF2 and $\phi_0 = 0.40$ for PF4. Configurations for higher β are qualitatively the same. The initial radius distribution is a uniform random distribution with $0.75 \leq R/R_m \leq 1.25$. The initial coordinate distribution is random. After an initial adjustment of radii, these systems satisfy $V_{\rm intra}(R) \simeq -[V_{\rm LSW}(R) + V_{\rm inter}(R)]$ and the total growth rate is $V_T \simeq 0$, for a wide interval of R. The final growth rate distribution for $\phi_0 = 0.40$ is depicted in Fig. 2(b). These systems are nearly frozen in a polydisperse liquid state. The concentration of defects also stays nearly constant. There is a strong coupling between the droplet radii and their positions and changing the radii or positions would alter the near cancellation of terms giving a net growth rate. Notice that $V_T = 0$ is not enough to get a metastable state because the equation for the radial growth is coupled to the equation for the motion of the centers of mass given by Eq. (47) and only when both $\dot{\mathbf{X}}_i = \mathbf{0}$ and $\dot{R}_i = 0$ will the system be metastable. One

TABLE II. Further runs in the monodisperse hexagonal regime. These runs correspond to film thickness $L = 10$ and volume fraction $\phi_0 = 0.04$. M is the mobility parameter, N_f is the average final number of droplets, n_d is the average final number of sites with coordination number different from 6, n_ρ is the defect decay exponent, $\tau_{\rm max}$ is the maximum time achieved in the simulation, and $n_{\rm run}$ is the number of independent quenches. The initial coordinate distribution (ICD) and initial radius distribution (IRD) are also indicated. All the configurations start with 500 droplets.

Run	β	M	ICD	IRD	N_f	n_d	n_ρ	$\tau_{\rm max}$	$n_{\rm run}$
MH1	0.36	1	random	$0.5 \leq R/R_m \leq 1.5$	343.75	20.8	0.46	176000	20
MH1b	0.36	10	random	$0.5 \leq R/R_m \leq 1.5$	370.35	17.7	0.43	42000	20
MH5	0.36	1	triangular	$0.75 \leq R/R_m \leq 1.25$	500	0		12800	10
MH6	0.36	1	random	$0.75 \leq R/R_m \leq 1.25$	422.60	90.40	0.50	12800	10
MH7	0.36	1	random	$R = R_{\rm eq}$	429.20	88.60	0.47	12800	10

TABLE III. Polydisperse frozen (PF) regime. L is the film thickness, β is the LRRI strength, ϕ_0 is the volume fraction, M is the mobility parameter. $\tau_{\max}$ is the maximum time achieved in the simulation, and n_{run} is the number of independent quenches.

Run	L	β	ϕ_0	M	$\tau_{\max}$	n_{run}
PF1	10	0.36	0.04	0.001	135000	8
PF2	10	0.08	0.04	0.001	381000	10
PF3	10	0.36	0.40	0.001	106000	4
PF4	10	0.08	0.40	0.001	544000	8

TABLE IV. Polydisperse coarsening (PC) regime. L is the film thickness, β is the LRRI strength, ϕ_0 is the volume fraction, M is the mobility parameter. $\tau_{\max}$ is the maximum time achieved in the simulation, and n_{run} is the number of independent quenches.

Run	L	β	ϕ_0	M	$\tau_{\max}$	n_{run}
PC1	1.5	0.36	0.04	4	200	10
PC2	2.5	0.08	0.04	4	900	10
PC3	1.5	0.36	0.40	2	1100	10
PC4	2.5	0.08	0.40	4	8000	10

way of getting $\dot{\mathbf{X}}_i$ negligible is by setting the mobility very low. Thus, if $M \to 0$ and $V_{\text{intra}} = -[V_{\text{LSW}} + V_{\text{inter}}]$ the system is kinetically frozen. Very small fluctuations in the growth rate around $V_T = 0$ [their amplitude cannot be seen in the scale of Fig. 2(b)] can lead this state to decay at very late times. In fact, for run PF4 at $\tau \sim 544\,000$ the number of droplets is approximately 95% of the number of droplets at $\tau = 0$ (for the small volume fraction runs, the number of droplets reaches a constant value very quickly). Simulations done with $M = 0$ exactly show that after an initial decay, the droplets adapt their size according to their relative position so that their number stays constant and the system is completely frozen. In any state where defects are stabilized, $V_T = 0$ due to the near cancellation $V_{\text{intra}} = -(V_{\text{LSW}} + V_{\text{inter}})$. Only in a perfect hexagonal state with equal radii is each of the three contributions exactly zero.

B. Coarsening behavior

Table IV gives different parameters used to test the polydisperse coarsening (PC) regime. Figure 6 shows typical configurations for runs PC2 and PC4, i.e., $L = 2.5$, $\beta = 0.08$, $M = 4$, and $\phi_0 = 0.04$ for PC2 and $\phi_0 = 0.40$ for PC4. Runs PC1 and PC3 give similar configurations. These systems are coarsening with growth exponents $n \sim 0.27$ for PC2 and $n \sim 0.29$ for PC4 (PC1 and PC3 have lower growth exponents, $n \sim 0.18$ and $n \sim 0.16$, respectively). The growth rate distribution for PC4 is shown in Fig. 2(c). Here $|V_{\text{LSW}}(R) + V_{\text{inter}}(R)| > |V_{\text{intra}}(R)|$ and the coupling of topological disorder and polydispersity contained in V_{inter} stabilizes the system as an evolving froth [8]. This case resembles the experimental results obtained for an amphiphilic monolayer by Seul *et al.* [8]. It also reproduces qualitatively the results obtained with previous Langevin simulations [12,13]. In fact, we found that the droplet distribution function computed for the latest time in the Langevin simulation follows closely the function shown here for run PC4. In the Langevin simulation we measured a growth exponent $n \sim 0.25$, although the scaling regime might not have been reached yet.

C. Droplet distribution

The hexagonal order contributes to the achievement of monodispersity. Polydisperse systems, on the other hand, can be stabilized through the coupling produced by I_{inter} between defects and the size of the constitutive droplets.

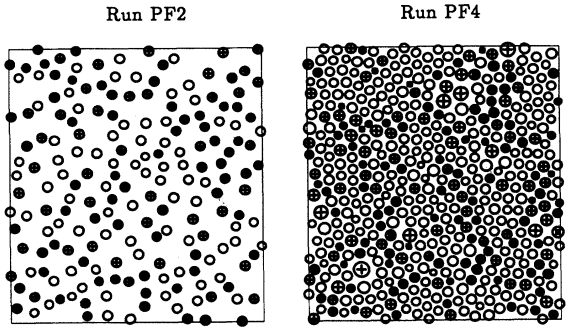

FIG. 5. Configurations for "frozen" runs PF2 and PF4: $L = 10$, $\beta = 0.08$, and $M = 0.001$; $\phi_0 = 0.04$ for PF2 and $\phi_0 = 0.40$ for PF4. The times for these configurations are $\tau = 381\,000$ and $\tau = 544\,000$, respectively. Droplets with coordination number $z < 6$ are indicated by filled symbols and those by $z > 6$ are indicated by a plus sign. The droplet areas in the configuration corresponding to PF2 have been enlarged by 4 to facilitate visualization.

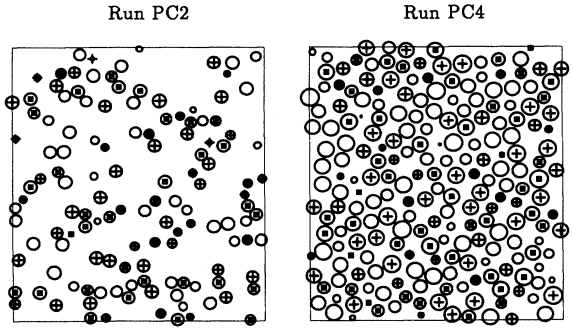

FIG. 6. Configurations for coarsening runs PC2 and PC4: $L = 2.5$, $\beta = 0.08$, and $M = 4$; $\phi_0 = 0.04$ for PC2 and $\phi_0 = 0.40$ for PC4. The times for these configurations are $\tau = 600$ and $\tau = 6000$, respectively. Droplets with coordination number $z < 6$ are indicated by filled symbols and those with $z > 6$ are indicated by a plus sign. The droplet areas in the configuration corresponding to PC2 have been enlarged by 4 to facilitate visualization.

Figure 7 shows the normalized average droplet distribution function $f(R/R_m)$, where R_m is the mean radius. Figure 7(a) depicts $f(R/R_m)$ for runs with volume fraction $\phi_0 = 0.04$. The left axis fixes the scale for the δ function corresponding to run MH1 and the right axis for the spread functions corresponding to runs PF2 (empty squares) and PC2 (solid circles). Figure 7(b) depicts $f(R/R_m)$ for runs with volume fraction $\phi_0 = 0.40$. The left axis fixes the scale for the spread functions corresponding to runs PF4 (empty squares) and PC4 (solid circles). The right axis fixes the scale for the sharp peak corresponding to run MH3. Runs with different dipolar strength β have similar behavior in each corresponding regime. Fewer spread functions with higher peaks correspond to smaller volume fractions. Runs corresponding to the polydisperse frozen regime are symmetric with respect to $R/R_m = 1$. Runs corresponding to the coarsening regime are more disperse and less symmetric than those in the frozen regime, their asymmetry growing with decreasing volume fraction.

Figure 8 shows the dependence of the average radius R_m on time. The classical LSW result [dashed line in Fig. 8(a)] has a growth exponent $n = 1/3$. Figure 8(a) depicts R_m for runs with volume fraction $\phi_0 = 0.04$ and Fig. 8(b) for runs with volume fraction $\phi_0 = 0.40$. For the monodisperse hexagonal regime, the growth of R_m stops once the δ function is reached. The solid line in (a) represents run MH2 and in (b) it represents run MH4. For the polydisperse frozen regime, R_m (represented by the open square symbols) is also constant. The filled circles show the results for the coarsening regime, where R_m has a growth exponent $n = 0.27$ for PC2 in (a) and $n = 0.29$ for PC4 in (b). The growth exponent measured in the different coarsening runs is nearly independent of volume fraction.

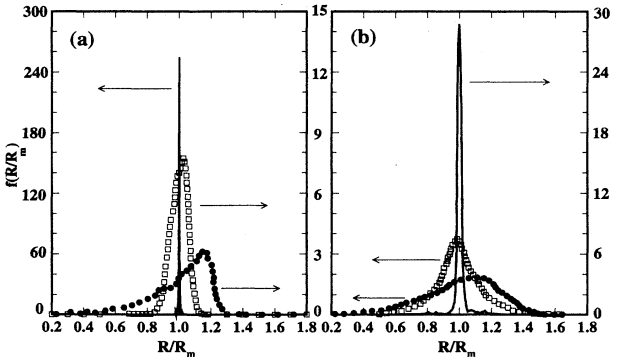

FIG. 7. Average droplet distribution function as a function of R/R_m. (a) Volume fraction $\phi_0 = 0.04$. The left axis fixes the scale for the δ function corresponding to run MH1 and the right axis for the spread functions corresponding to runs PF2 (empty squares) and PC2 (solid circles). (b) Volume fraction $\phi_0 = 0.40$. The left axis fixes the scale for the spread functions corresponding to runs PF4 (empty squares) and PC4 (solid circles). This axis is common to (a) and (b). The right axis fixes the scale for the sharp peak corresponding to run MH3.

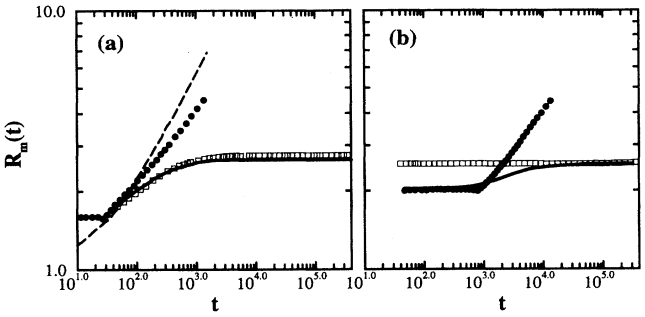

FIG. 8. Average radius R_m as a function of time. (a) Volume fraction $\phi_0 = 0.04$. Dashed line, classical LSW result; open squares, run PF2; filled circles, run PC2; solid line, run MH2. (b) Volume fraction $\phi_0 = 0.40$. These curves are multiplied by 0.4 to facilitate comparison with (a). Open squares, run PF4; filled circles, run PC4; solid line, run MH4.

D. Defect annealing dynamics

The mechanisms of defect collision and annhilation or creation are the same as those described in a Langevin simulation study [12,13]. Voronoi constructions have been used to isolate the topological defects. Disclinations of charge q are characterized by a mismatch of $q\pi/3$ in the orientation angle after a lattice circuit. Alternatively, they can be considered as a site with a wrong number of nearest neighbors as measured by the Voronoi polygon construction. If their coordination number is z, then their charge can also be expressed as $q = z - 6$. All of the observed defect collision mechanisms correspond to a T_1 process, a T_2 process, or different combinations of the elementary T_1 and T_2 processes [13]. While the concentration of topological defects decays in the monodisperse hexagonal regime, it stays nearly constant in the polydisperse regimes.

At late stages in the monodisperse hexagonal regime, the majority of droplets have coordination number $z = 6$, while a smaller number have $z = 5$ (topological charge $q = -1$) and an equal number have $z = 7$ ($q = +1$); the early stages present a small number of disclinations with higher charge. Isolated disclinations with opposite topological charge attract each other strongly and form clusters that correspond to more complex topological defects. The fivefold and sevenfold disclinations often occur in local pairs as edge dislocations, which correspond to two additional half rows of droplets. The Burgers vector is defined as the amount by which a path around the dislocation core fails to close. It lies along the direction perpendicular to the line joining the bound-disclination pair, known as the glide direction. Dislocations move relatively easily in the glide direction, but less easily in the climb direction, perpendicular to the Burgers vector.

The time evolution of the monodisperse hexagonal systems found in the simulations is characteristic of 2D freezing: starting from the liquid state, the systems order both orientationally and positionally towards the crystalline state. To quantify the two types of ordering, we have measured the normalized structure factor $S(k,\theta)$,

the orientational order parameter f_6 as defined below by Eqs. (76) and (77), which produce essentially the same curve, and the translational order parameter f_T as defined below by Eq. (73).

The crystal translational order parameter is the local Fourier component of the density [23],

$$\rho_{\mathbf{K}}(\mathbf{x}) = e^{i\mathbf{K}\cdot\mathbf{x}} , \tag{72}$$

where $\mathbf{K}$ is a reciprocal lattice vector to the first Bragg peak in the structure factor of the crystal. This order parameter is complex, continuous, and Abelian. In 2D solids there is no long-range order, only quasi-long-range translational order. The mean translational order parameter of the infinite crystal is zero, but its correlation function decays algebraically in space with a temperature-dependent decay exponent.

For the simulations, to show the time evolution of translational order, we consider the quantity f_T defined as

$$f_T = \left| \left\langle \frac{1}{N_T} \sum_{i=1}^{N_T} e^{i\mathbf{K}\cdot\mathbf{X}_i} \right\rangle \right|, \tag{73}$$

where $\mathbf{X}_i$ is the center-of-mass coordinate of droplet i, $\mathbf{K}$ is the reciprocal lattice vector to the first Bragg peak, and the sum is over the centers of the N_T droplets. The angular brackets denote an average over the six directions in $\mathbf{K}$ [24].

Orientational order in two dimensions is measured via a complex, $\mathbf{x}$-dependent orientational order parameter defined as [25]

$$\psi_6(\mathbf{X}_i) = \frac{1}{N_i} \sum_{j=1}^{N_i} e^{i6\theta_j(\mathbf{X}_i)} , \tag{74}$$

where $\mathbf{X}_i$ is the center-of-mass coordinate of droplet i and N_i is the number of nearest neighbors of droplet i; the sum is over all the nearest-neighbor bonds. A quantitative measure of orientational order is provided by the correlation function

$$g_6(x) = \langle \psi_6^*(\mathbf{x})\psi_6(\mathbf{0}) \rangle, \tag{75}$$

where the angular brackets represent an average over all pairs of droplets separated by x and an angular average over $\pi/3$-rad segments.

To study the time evolution of the orientational order, we consider the quantity f_6 defined as [25]

$$f_6 = \left| \left\langle \frac{1}{N_i} \sum_{j=1}^{N_i} e^{i6\theta_j(\mathbf{X}_i)} \right\rangle \right|. \tag{76}$$

The definition of the orientational order parameter used in analyzing various experiments [26] is carried out in Fourier space. The equivalent of Eq. (76) is

$$f_6 = \left| \sum_{k,\theta} S(k,\theta)\, e^{i6\theta} \right|, \tag{77}$$

where $S(k,\theta)$ is the normalized structure factor. Another definition of the orientational order parameter often used is $f_6' = [g_6(0)]^{1/2}$, that is,

$$f_6' = \left\langle \left| \frac{1}{N_i} \sum_{j=1}^{N_i} e^{i6\theta_j(\mathbf{X}_i)} \right|^2 \right\rangle^{\frac{1}{2}} . \tag{78}$$

This second definition, however, is a measure of local order, in the sense that it contains no information about correlations between bonds separated by large distances. Equations (76) and (77) give essentially the same results, while naturally, Eq. (78) gives higher values. Both definitions give $f_6' = f_6 = 1$ in a perfect crystalline solid.

We have also measured the concentration of defects $\rho(\tau)$ defined as the ratio of the number of droplets with $z \neq 6$ to the total number of droplets N_T: $\rho(\tau) = 1 - C_6$, where $C_6 = N_6/N_T$ is the concentration of sixfold coordinated droplets. The orientational order parameter f_6' defined by Eq. (78) produces results that follow closely those for C_6.

Figure 9 shows the time evolution of the orientational and translational order parameters f_6, f_6', and f_T and the defect concentration $\rho(\tau)$ for runs MH1b, MH1, and MH3. These runs have film thickness $L = 10$ and dipolar strength $\beta = 0.36$. Runs MH1b and MH1 correspond to volume fraction $\phi_0 = 0.04$ and run MH3 to volume fraction $\phi_0 = 0.40$. Inspection of the configurations corresponding to individual runs indicates that in those runs with grain boundaries, orientational and translational or-

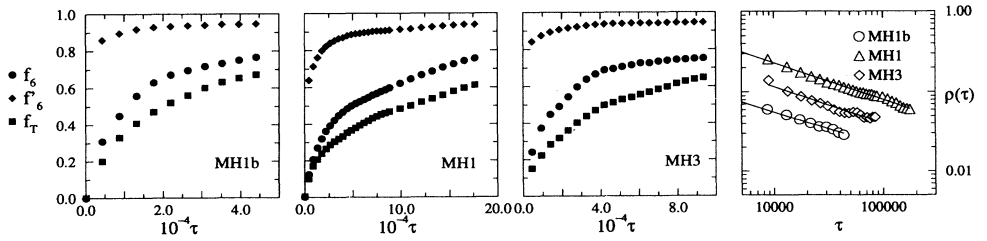

FIG. 9. Orientational order parameters f_6, f_6' and translational order parameter f_T for runs MH1b, MH1, and MH3. The fourth panel represents the defect decay for these runs. The measured decay exponent is $n = 0.43$ for MH1b, $n = 0.46$ for MH1, and $n = 0.46$ for MH3. To facilitate visualization, the data points for MH1b have been multiplied by 0.6.

ders are disrupted, while in those runs without grain boundaries, the onset of quasi-long-range orientational order occurs sooner than the onset of quasi-long-range positional order. In such cases, the system evolves in time through intermediate stages of hexatic order before reaching the crystalline state. Since there is a wide variation in the values of the order parameters for different runs, an average over many runs is required. The average values of f_6 and f_T shown in this figure indicate that at any given time (except at very early times) the average orientational order parameter is higher than the average translational order parameter. A comparison between MH1 (M=1) and MH1b (M=10) confirms that systems with higher values of the mobility parameter attain orientational and translational order sooner than lower values of M. Runs with lower β take longer to reach equal values of f_6 and f_T. The last panel in Fig. 9 shows the decay of the defect concentration $\rho(\tau)$. The measured decay exponent is $n_\rho = 0.43$ for MH1b, $n_\rho = 0.46$ for MH1, and $n_\rho = 0.46$ for MH3. These values are consistent with a decay exponent $n_\rho \simeq 0.5$. We attribute this value [13] to the fact that the dislocations in our simulations are not distributed uniformly in regions of linear dimension L but rather on the surface or the contour of this region. Suppose L is the characteristic linear dimension of the ordered domains that compete to select the ground state. Let $V(L)$ be the potential that characterizes the interaction of the relevant defects. The motion of defects in the simplest case is characterized by a Langevin equation $dL/d\tau \sim -dV(L)/dL$. Point defects in two dimensions interact logarithmically, so the integration of the Langevin equation gives $L(\tau) \sim \tau^{1/2}$. [In two dimensions, for order parameters with two components there is a logarithmic correction [27] $L(\tau) \sim (\tau/\ln\tau)^{1/2}$.] If the dislocations are distributed at the surface of the ordered regions, then $\rho(\tau) \sim \left[L(\tau)\right]^{-1} \sim \tau^{-1/2}$. (If, on the other hand, the defects were uniformly distributed, the concentration of defects would verify $\rho(\tau) \sim \left[L(\tau)\right]^{-2} \sim \tau^{-1}$.) Further simulations or experimental studies would be necessary to determine exactly the decay exponent for these particular systems.

E. Statistical analysis of polydisperse configurations

In contrast to the monodisperse hexagonal regime, the droplet patterns in the polydisperse regime (Figs. 5 and 6) retain a high concentration of topological defects $N_{z\neq 6}/N \geq 0.5$. Their geometrical and topological statistics give them properties of cellular patterns or froths [28]. A system such as that described by the coarsening runs is believed to verify von Neumann's law [29], which states that the area of a froth cell increases with time if $z-6>0$ or decreases if $z-6<0$, $\dot{A} = k(n-6)$. Instead, in the monodisperse case this area remains constant. At late stages, in froths the T_2 processes are dominant and the T_1 processes are very rare. In monodisperse hexagonal systems, on the other hand, the T_1 processes are the dominant mechanism.

We further analyze the statistical aspects of polydisperse configurations using the maximum entropy formalism as introduced by Rivier [30] and extended by Seul, Sire, and Morgan (SSM) [8] for a Langmuir monolayer. First, we recapitulate the main features of this formalism. Let $\langle S_B\rangle$ and $\langle A\rangle$ be the average droplet area ($\langle S_B\rangle \sim t^{2n}$) and the average Voronoi cell area. Let $P_n(a,s)$ be the probability of finding a droplet of area $S_B = s\langle S_B\rangle$ in an n-sided Voronoi cell of area $A = a\langle A\rangle$ (thus $\langle a\rangle = 1$ and $\langle s\rangle = 1$). Let p_n be the density of n-sided Voronoi cells $p_n = \int da\, ds P_n(a,s)$ and a_n and s_n be the averages of a and s for these cells: $a_n = \frac{1}{p_n}\int da\ ds\ a\ P_n(a,s)$, and similarly for s_n. One defines the entropy in terms of the probability $P_n(a,s)$ and maximizes the entropy subject to the following constraints: (i) normalization of probability,

$$\sum_{n\geq d+1} p_n = 1; \tag{79}$$

(ii) space-filling froth structure,

$$\sum_{n\geq d+1} p_n a_n = 1; \tag{80}$$

(iii) charge neutrality,

$$\sum_{n\geq d+1} p_n (n-6) = 0; \tag{81}$$

(iv) conservation of energy,

$$\sum_{n\geq d+1} p_n (n-6)^2 = \mu_2, \tag{82}$$

where μ_2 is the second moment of the distribution p_n and the moments are defined as $\mu_\alpha = \sum_{n\geq d+1} p_n (n-6)^\alpha$ ($\mu_0 = 1$ and $\mu_1 = 0$); (v) conservation of mass,

$$\sum_{n\geq d+1} p_n s_n = 1; \tag{83}$$

and (vi) each Voronoi cell contains exactly one droplet,

$$\phi_0 s_n < a_n. \tag{84}$$

One can maximize the entropy as a function of a_n and s_n with the given constraints. If these constraints are relaxed, then there is more arbitrariness in the distribution $\{p_n\}$. Rivier and Lissowski showed that Lewis's law corresponds to "maximal arbitrariness" in this distribution, obtained by making one of the constraint equations a linear combination of the others. Thus one can write

$$a_n = 1 + \lambda_a(n-6) + \nu_a\left[(n-6)^2 - \mu_2\right], \tag{85}$$

$$s_n = 1 + \lambda_s(n-6) + \nu_s\left[(n-6)^2 - \mu_2\right]. \tag{86}$$

In cells with strong energetic constraints, the quadratic term is expected to dominate while in coarsening droplet patterns, ν_a and ν_s are expected to give a negligible contribution (Lewis's law is just the linear part of these equations).

TABLE V. Lewis's law coefficients λ_s, ν_s, λ_a, and ν_a, the second moment of the probability distribution μ_2, and the growth exponent n.

Run	λ_s	ν_s	λ_a	ν_a	μ_2	n
PC1	0.03	0	0.18	0	1.23	0.18
PC2	0.01	0	0.16	0	1.29	0.27
PC3	0.18	0.03	0.12	0	0.61	0.16
PC4	0.11	0	0.12	0	0.68	0.29
PF1	0.04	0.01	0.14	0.01	0.92	0
PF2	0.04	0	0.13	0	0.92	0
PF3	0.18	0.04	0.08	0.02	0.34	0
PF4	0.31	0.10	0.14	0.04	0.44	0

Finally, the Aboav-Weaire law [28] describes the correlations in the topological charge of nearest-neighbor cells. If $m(n)$ is the average coordination number of the n nearest-neighbor cells of the n-sided cell, the Aboav-Weaire law reads

$$nm(n) = (6 - \zeta)(n - 6) + 36 + \mu_2 \ , \qquad (87)$$

where ζ is a phenomenological constant.

Table V gives the Lewis law coefficients $\lambda_s, \nu_s, \lambda_a, \nu_a$, the second moment of the probability distribution μ_2, and the growth exponent n. For the coarsening runs, Lewis's law is strictly valid for the Voronoi cells, i.e., Eq. (85) is linear. Figure 10(a) (empty squares) shows this relation for run PC3. This same run presents a small quadratic contribution in Eq. (86) for the droplet areas (filled squares). Most of the frozen runs present a small quadratic contribution in the Voronoi cell equation as well as in the droplet area equation (except for run PF2). Figure 10(a) also shows Eqs. (85) (empty circles) and (86) (filled circles) for run PF3 (displaced in vertical direction by 0.5 for clarity). The quadratic contribution is more important in run PF4. SSM considered that the parameter λ_s is a susceptibility that determines the change in the average droplet area due to a change in the coordination number (or, equivalently, the magnitude of the geometrical response due to variations of a topological quantity). They concluded that due to the linear correlation between droplet areas and topological charge, the screening of charge precludes large fluctuations in the area of the droplet. Thus, as the volume fraction decreases, the value of λ_s also decreases, as shown in Table II. Figure 10(b) shows Aboav-Weaire law for runs PC3 (squares) and PF3 (circles). The linear behavior is seen as expected.

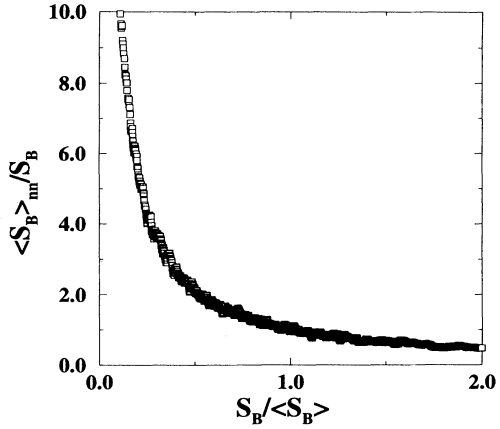

FIG. 11. Spatial correlations in the areas of nearest-neighbor droplets for run PC4. $\langle S_B \rangle_{nn}$ represents the average area of droplets that are nearest neighbors to a given droplet.

Figure 11 shows the spatial correlations in the areas of nearest-neighbor droplets for run PC4. There is a strong anticorrelation due to the screening of charge and of area fluctuations.

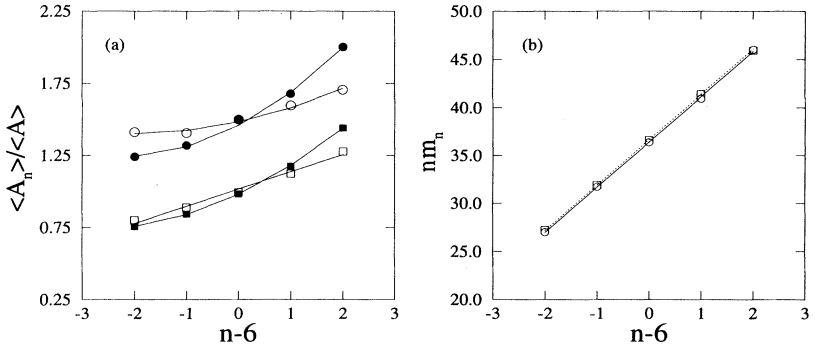

FIG. 10. (a) Lewis' law. (b) Aboav-Weaire law. In these plots n is the droplet coordination number and m_n is the average coordination number of the nearest-neighbor droplets of an n-fold droplet. In (a), $\langle A \rangle$ and $\langle A_n \rangle$ respectively represent the average area of Voronoi cells and the average area of n-sided Voronoi cells for the empty symbols; for the filled symbols, they represent the average droplet area and the average area of n-fold coordinated droplets. The square data points in (a) and (b) correspond to run PC3 and the circular data points in (a) and (b) correspond to run PF3. In (a) the curves intersect at $n - 6 = 0$, but the circular data points have been displaced 0.5 in the vertical direction to facilitate visualization.

V. SUMMARY

In this paper we have studied the effects of a LRRI on the classical coarsening mechanism of Lifshitz, Slyozov, and Wagner. Starting from the Ginzburg-Landau free energy and a Langevin dynamical equation for the order parameter, we derived a set of interface equations that couple growth and motion of droplets. The resulting multidroplet diffusion equation was integrated numerically under the monopole approximation. We found a noncoarsening and a coarsening regime. In the noncoarsening regime, the system is history dependent and sensitive to the magnitude of the hexagonal order present in the early stages. Monodispersity is aided by hexagonal order. If hexagonal order is hindered, the system is stabilized— through the coupling produced by interdroplet interactions $I_{\rm inter}$ between the positions and sizes of droplets—as a kinetically frozen polydisperse liquid, where the mean radius is constant in time. In the coarsening regime, the coupling of topological disorder and polydispersity stabilizes the system as an *evolving* froth, which coarsens with a reduced growth exponent.

ACKNOWLEDGMENTS

We acknowledge the support from the NSERC of Canada. We would also like to thank Chuck Yeung for useful discussions.

APPENDIX

In this appendix we derive the interfacial equations using the method of matched asymptotic expansions [15–17]. The system is partitioned into bulk (outer) and interfacial (inner) regions. The interfacial region is defined as a skin around the interface Γ of thickness larger than $O(1)$ but less than the macroscopic lengths, which are $O(1/\epsilon)$. The bulk region can be divided in two subregions Ω_- and Ω_+ characterized by negative and positive values of the order parameter and separated by the interface Γ. The order parameter and the chemical potential are expanded in ϵ to the different orders. Differential equations for ψ and μ are obtained for different orders in each region and matched to the same order at the boundary between the regions.

Near the interface, it is useful to use curvilinear coordinates. Let s represent a set of $(d-1)$ coordinates along the interface and $\hat{\mathbf{s}}$ represent the set of tangent vectors to the interface. Let $\hat{\mathbf{u}}$ be the normal vector at the interface point $\mathbf{r}(s)$ specified by the contour variable s and u the coordinate along that direction. Not too far from the interface a bulk point $\mathbf{x}$ can be represented by the curvilinear coordinates (s,u) where $\mathbf{x}=\mathbf{r}(s)+u\hat{\mathbf{u}}$. The normal $\hat{\mathbf{u}}$ to the front Γ points from Ω_- to Ω_+. The mean curvature of the front Γ is defined as $\kappa=\nabla\cdot\hat{\mathbf{u}}$ and it is positive if the center of curvature lies in Ω_-. The normal velocity of the front is defined as $v=\partial u/\partial\tau$ and it is positive if the front moves towards Ω_-.

In the outer region (bulk) all the distances are rescaled as $\mathbf{X}=\epsilon\mathbf{x}$; in particular, the coordinates parallel and normal to the interface are $S=\epsilon s$ and $W=\epsilon u$. Since we are interested in structures much larger than the interfacial width, these coordinates are time independent. In the inner region, the coordinates parallel to the interface are also $S=\epsilon s$, while the normal coordinate is $w=u$. To match the outer and inner solutions at the boundary, one has to take the limit $\epsilon\to 0$, which corresponds to matching the outer solution at small W to the inner solution at large w. For the inner expansion, the gradient can be written as $\nabla_x=\hat{\mathbf{w}}\partial_w+\epsilon\hat{\mathbf{s}}\partial_S$. By using the Frenet equations [31] $\partial_s\hat{\mathbf{s}}=-\kappa\hat{\mathbf{u}}$ and $\partial_s\hat{\mathbf{u}}=\kappa\hat{s}$, and assuming that the tangential component does not depend on the normal distance (i.e., $\partial_w\hat{\mathbf{s}}=\mathbf{0}$), we get for the Laplacian in the inner region

$$\nabla_x^2=\frac{\partial^2}{\partial w^2}+\epsilon\tilde{\kappa}\frac{\partial}{\partial w}+\epsilon^2\frac{\partial^2}{\partial S^2}, \tag{A1}$$

where $\tilde{\kappa}=\kappa/\epsilon$ is the rescaled curvature.

Time is rescaled as $T=\epsilon^3\tau$ to extract the long time behavior. The rescaled velocity V is given by $v=\epsilon^2V$. For the inner region, the coordinate system is no longer time independent; it must take into account that the interface is moving. Thus the time derivative can be written as

$$\frac{\partial}{\partial\tau}=\epsilon^3\left.\frac{\partial}{\partial T}\right|_{S,w}+\epsilon^2V\frac{\partial}{\partial w}, \tag{A2}$$

where we have chosen to set $\partial S/\partial\tau=0$ since we are always free to reparametrize s about each point.

For the order parameter and chemical potential, the outer expansion is

$$\psi=\psi_0+\epsilon\psi_1+\epsilon^2\psi_2+\cdots, \tag{A3}$$

$$\mu=\mu_0+\epsilon\mu_1+\epsilon^2\mu_2+\cdots, \tag{A4}$$

$$\mu_0=f'(\psi_0)=\mu_B(\psi_0)\ ,$$

$$\mu_1=f''(\psi_0)\psi_1\ ,$$

$$\mu_2=\frac{1}{2}f'''(\psi_0)\psi_1^2+f''(\psi_0)\psi_2-\nabla_X^2\psi_0\ , \tag{A5}$$

where ψ_0 is the bulk solution, far from the interface. The inner expansion is

$$\tilde{\psi}=\tilde{\psi}_0+\epsilon\tilde{\psi}_1+\epsilon^2\tilde{\psi}_2+\cdots, \tag{A6}$$

$$\tilde{\mu}=\tilde{\mu}_0+\epsilon\tilde{\mu}_1+\epsilon^2\tilde{\mu}_2+\cdots, \tag{A7}$$

$$\tilde{\mu}_0=f'(\tilde{\psi}_0)-\partial_w^2\tilde{\psi}_0\ ,$$

$$\tilde{\mu}_1=f''(\tilde{\psi}_0)\tilde{\psi}_1-\partial_w^2\tilde{\psi}_1-\tilde{\kappa}\partial_w\tilde{\psi}_0\ ,$$

$$\tilde{\mu}_2=\frac{1}{2}f'''(\tilde{\psi}_0)\tilde{\psi}_1^2+f''(\tilde{\psi}_0)\tilde{\psi}_2-\partial_w^2\tilde{\psi}_2-\tilde{\kappa}\partial_w\tilde{\psi}_1-\partial_S^2\tilde{\psi}_0\ . \tag{A8}$$

Finally, the inner and outer solutions have to be matched to the same order at the boundary. We require that the chemical potential be the same, which means that to every order

$$\mu_i = \tilde{\mu}_i \tag{A9}$$

or, equivalently,

$$\psi_i = \tilde{\psi}_i \tag{A10}$$

and that the normal derivatives match at the same order at the interface

$$\partial_W^n \mu_i = \partial_w^n \tilde{\mu}_{i+n} \tag{A11}$$

or, equivalently,

$$\partial_W^n \psi_i = \partial_w^n \tilde{\psi}_{i+n}. \tag{A12}$$

Now we apply the dynamical expansion to Eq. (2):

$$\frac{\partial\psi(\mathbf{x},\tau)}{\partial\tau} = \nabla^2\left[\mu + \beta\int d^dx' g(|\mathbf{x}-\mathbf{x}'|)\psi(\mathbf{x}',\tau)\right]. \tag{A13}$$

The dynamical equation in the outer region becomes

$$\epsilon^3\frac{\partial\psi}{\partial T} = \epsilon^2\nabla_X^2\left[\mu(\psi) + \beta\epsilon\int_{\text{out}} d^dX' g(|\mathbf{X}-\mathbf{X}'|)\psi(\mathbf{X}') + \beta\epsilon^2\int_\Gamma d^{d-1}S'\int_{-\infty}^{\infty} dw' g((S-S')^2 + (W-\epsilon w')^2)\tilde{\psi}(S',w')\right] \tag{A14}$$

and in the inner region it becomes

$$\epsilon^3\frac{\partial\tilde{\psi}}{\partial T} + \epsilon^2 V\frac{\partial\tilde{\psi}}{\partial w} = (\partial_w^2 + \epsilon\tilde{\kappa}\partial_w + \epsilon^2\partial_s^2)\left[\tilde{\mu}(\tilde{\psi}) + \beta\epsilon\int_{\text{out}} d^dX' g((S-S')^2 + (\epsilon w - W')^2)\psi(\mathbf{X}') + \beta\epsilon^2\int_\Gamma d^{d-1}S'\int_{-\infty}^{\infty} dw' g((S-S')^2 + \epsilon^2(w-w')^2)\tilde{\psi}(S',w')\right]. \tag{A15}$$

Now we obtain a macroscopic description of interfacial dynamics to first order in the expansion.

1. Zeroth order

In the outer region the dynamical equation to lowest order in ϵ (i.e., ϵ^2) is

$$\nabla_X^2\mu_B(\psi_0) = 0. \tag{A16}$$

The outer solution is given by the equilibrium solution $\mu_0 = 0$ and $\psi_0 = +\psi_{\text{eq}}$ in Ω_+ and $\psi_0 = -\psi_{\text{eq}}$ in Ω_-. In the inner region the lowest-order (ϵ^0) dynamical equation is

$$\partial_w^2\tilde{\mu}_0 = \partial_w^2[\tilde{\mu}_B(\tilde{\psi}_0) - \partial_w^2\tilde{\psi}_0] = 0. \tag{A17}$$

This last equation means $\tilde{\mu}_0 = a + bw$. $\tilde{\mu}_0$ and $\tilde{\psi}_0$ must match the outer solution at $w \gg 1$; since $\tilde{\mu}_0$ has to be finite, this requires $b = 0$. (Otherwise, $\partial_W\mu_{-1} = \partial_w\tilde{\mu}_0 = b = 0$.) The other matching condition $\mu_0 = \tilde{\mu}_0$ gives $a = 0$. Thus $\mu_0 = \tilde{\mu}_0 = 0$ in all space and the solution of $0 = f'(\tilde{\psi}_0) - \partial_w^2\tilde{\psi}_0$ is the planar interface solution $\tilde{\psi}_0 = \tilde{\psi}_0(w)$.

2. First order

In the outer region the dynamical equation to order ϵ^3 gives $\partial\psi_0/\partial T = 0$ or

$$\nabla_X^2\left[\mu_1 + \beta\int_{\text{out}} d^dX' g(|\mathbf{X}-\mathbf{X}'|)\psi_0(\mathbf{X}')\right] = 0, \tag{A18}$$

where $\mu_1 = \mu_B'(\psi_0)\psi_1 = \chi^{-1}\psi_1$ and $\chi = (\partial\mu/\partial\psi)_{\text{eq}}^{-1}$ is the susceptibility. This is the equation describing the bulk dynamics of the order parameter field to first order in ϵ. At this order, the quasistatic approximation $\partial\psi/\partial T = 0$ in the bulk is valid.

In the inner region the next order (ϵ^1) dynamical equation is

$$\partial_w^2\tilde{\mu}_1 + \tilde{\kappa}\partial_w\tilde{\mu}_0 = 0. \tag{A19}$$

We use the zeroth-order result $\tilde{\mu}_0 = 0$ and integrate Eq. (A19) across the interface. By using the matching condition $\partial_w\tilde{\mu}_1|_\Gamma = \partial_W\mu_0|_\Gamma = 0$ we get that $\tilde{\mu}_1 = \tilde{\mu}_1(s)$, i.e., $\tilde{\mu}_1$ is only a function of the contour coordinates

$$\tilde{\mu}_1(s) = \tilde{\mu}_B'(\tilde{\psi}_0)\tilde{\psi}_1 - \partial_w^2\tilde{\psi}_1 - \tilde{\kappa}\partial_w\tilde{\psi}_0. \tag{A20}$$

We multiply both sides of this equation by $\partial_w\tilde{\psi}_0$ and integrate over the interface

$$\tilde{\mu}_1(s)\int dw\partial_w\tilde{\psi}_0 = \int dw\partial_w\tilde{\psi}_0(\tilde{\mu}_B' - \partial_w^2)\tilde{\psi}_1 - \tilde{\kappa}\int dw(\partial_w\tilde{\psi}_0)^2. \tag{A21}$$

The function $\partial_w\tilde{\psi}_0$ is the Goldstone mode corresponding to a translation of the interface. The first term on the rhs vanishes after integration by parts since the Goldstone mode is a zero eigenvector of the linear operator $\tilde{\mu}_B' - \partial_w^2$. The surface tension σ is given by $\sigma = \int dw(\partial_w\tilde{\psi}_0)^2$. The previous equation becomes

$$\tilde{\mu}_1(s)\Delta\psi_{\text{eq}} = -\tilde{\kappa}(s)\sigma. \tag{A22}$$

Applying the matching condition $\mu_1|_\Gamma = \tilde{\mu}_1(s)|_\Gamma$,

$$\mu_1|_\Gamma = -\frac{\tilde{\kappa}(s)\sigma}{\Delta\psi_{\text{eq}}}. \tag{A23}$$

This is the Gibbs-Thomson boundary condition, which arises from a statement of local equilibrium and expresses the fact that the order parameter near a curved interface is determined by the local curvature and the local surface tension.

3. Second order

To complete the first-order description in the bulk, we must obtain $\partial_w \tilde{\mu}_2$ in the inner solution evaluated at large w. The dynamical equation for the inner expansion to second order (ϵ^2) is

$$V\partial_w \tilde{\psi}_0 = \partial_w^2 \tilde{\mu}_2 + \tilde{\kappa}\partial_w \tilde{\mu}_1 + \partial_S^2 \tilde{\mu}_0. \quad \text{(A24)}$$

Taking into account that $\partial_w \tilde{\mu}_1 = 0$ and $\tilde{\mu}_0 = 0$, we integrate this equation across the interface

$$V\Delta\psi_{\rm eq} = \left[\partial_w \tilde{\mu}_2\right]_\Gamma = \left[\partial_W \mu_1\right]_\Gamma = \left[\hat{\mathbf{u}} \cdot \nabla_x \mu_1\right]_\Gamma. \quad \text{(A25)}$$

This equation expresses the fact that the normal velocity of the interface is proportional to the discontinuity of the chemical potential across the interface.

We return to the original unrescaled variables $\mu = \epsilon\mu_1$, $v = \epsilon^2 V$, $\kappa = \epsilon\tilde{\kappa}$, etc., and call the normal $\hat{\mathbf{n}}$ ($\hat{\mathbf{n}} = \hat{\mathbf{u}}$). We obtain as the final set of equations Eqs. (6)–(8).

[1] I.M. Lifshitz and V.V. Slyozov, J. Phys. Chem. Solids **19**, 35 (1961).

[2] C. Wagner, Z. Electrochem. **65**, 581 (1961).

[3] J.A. Marqusee and J. Ross, J. Chem. Phys. **80**, 536 (1984); P.W. Voorhees, J. Stat. Phys. **38**, 231 (1985); C.W.J. Beenaker, Phys. Rev. A **33**, 4482 (1986); Y. Enomoto, M. Tokuyama, and K. Kawasaki, Acta Metall. **34**, 2119 (1986); M. Marder, Phys. Rev. A **36**, 858 (1987); A.J. Ardell, Phys. Rev. B **41**, 2554 (1990); J.H. Yao, K.R. Elder, H. Guo, and M. Grant, *ibid.* **45**, 8173 (1992).

[4] L. Leibler, Macromolecules **13**, 1602 (1980); T. Ohta and K. Kawasaki, *ibid.* **19**, 2621 (1986); Y. Oono and M. Bahiana, Phys. Rev. Lett. **61**, 1109 (1988).

[5] R.E. Rosensweig, M. Zahn, and R. Shumovich, J. Magn. Magn. Mater. **39**, 127 (1983).

[6] C.A. Murray and D.H. Van Winkle, Phys. Rev. Lett. **58**, 1200 (1987); C.A. Murray and R.A. Wenk, *ibid.* **62**, 1643 (1989); C.A. Murray, W.O. Sprenger, and R.A. Wenk, Phys. Rev. B **42**, 688 (1990).

[7] M. Seul and C.A. Murray, Science **262**, 558 (1993); M. Seul, J. Phys. (France) I **4**, 319 (1994).

[8] M. Seul, N.Y. Morgan, and C. Sire, Phys. Rev. Lett. **73**, 2284 (1994); M. Seul, Europhys. Lett. **28**, 557 (1994); N.Y. Morgan and M. Seul, J. Phys. Chem. **99**, 2088 (1995); C. Sire and M. Seul, J. Phys. (France) I **5**, 97 (1995).

[9] C. Roland and R.C. Desai, Phys. Rev. B **42**, 6658 (1990).

[10] R.C. Desai, C. Sagui, and K.R. Elder, in *Structure and Dynamics of Strongly Interacting Colloids and Supramolecular Aggregates in Solution*, edited by S.H. Chen *et al.* (Kluwer, Dordrecht, 1992), p. 205.

[11] C. Sagui and R.C. Desai, Phys. Rev. E **49**, 2225 (1994).

[12] C. Sagui and R.C. Desai, Phys. Rev. Lett. **71**, 3995 (1993).

[13] C. Sagui and R.C. Desai, Phys. Rev. E **52**, 2807 (1995).

[14] C. Sagui and R.C. Desai, Phys. Rev. Lett. **74**, 1119 (1995).

[15] G. Caginalp, Ann. Phys. (N.Y.) **172**, 136 (1986); G. Caginalp and P.C. Fife, SIAM (Soc. Ind. Appl. Math.) J. Appl. Math. **48**, 506 (1988); G. Caginalp, Phys. Rev. A **39**, 5887 (1989).

[16] R.L. Pego, Proc. R. Soc. London Ser. A **422**, 261 (1989).

[17] C. Yeung, J.L. Mozos, A. Hernández-Machado, and D. Jasnow, J. Stat. Phys. **70**, 1149 (1993); C. Yeung and R.C. Desai, Phys. Rev. E **49**, 2096 (1994).

[18] N. Akaiwa and P.W. Voorhees, Phys. Rev. E **49**, 3860 (1994); N. Akaiwa and D.I. Meiron, *ibid.* **51**, 5408 (1995).

[19] P.W. Voorhees and M.E. Glicksman, Acta Metall. **32**, 2001 (1984); **32**, 2013 (1984); J.H. Yao, K.R. Elder, H. Guo, and M. Grant, Phys. Rev. B **47**, 14110 (1993).

[20] I.S. Gradshteyn and I.M. Ryzhik, in *Table of Integrals, Series and Products*, edited by A. Jeffrey (Academic, New York, 1980).

[21] H.M. McConnell, Proc. Natl. Acad. Sci. U.S.A. **86**, 3452 (1989).

[22] These considerations are valid for lattice constants near the equilibrium value, where the system is stable or metastable. Far from equilibrium, the system is strained and can become unstable.

[23] D.R. Nelson, in *Phase Transitions and Critical Phenomena*, edited by C. Domb and J. K. Lebowitz (Academic, New York, 1983), Vol. 7, p. 2.

[24] Note that in this definition the angular brackets and the absolute value bars are in different order compared to the definition in Refs. [12,13]. The present definition takes into account all the interference effects, as does the definition for the orientational order parameter in Eq. (76). Consequently the function f_T in Refs. [12,13] has higher values than it would have with the definition in Eq. (73).

[25] D. Frenkel and J.P. McTague, Phys. Rev. Lett. **42**, 1632 (1979).

[26] R.J. Birgeneau and J.D. Litster, J. Phys. (Paris) Lett. **38**, 1399 (1978); D.E. Moncton and R. Pindak, Phys. Rev. Lett. **43**, 701 (1979); J.D. Brock, A. Aharony, R.J. Birgeneau, K.W. Evans-Lutterodt, J.D. Litster, P.M. Horn, G.B. Stephenson, and A.R. Tajbakhsh, *ibid.* **57**, 98 (1986).

[27] A.N. Pargellis, P. Finn, J.W. Goodby, P. Pannizza, B. Yurke, and P.E. Cladis, Phys. Rev. A **46**, 7765 (1992).

[28] D. Weaire and N. Rivier, Contemp. Phys. **25**, 59 (1984).

[29] M.O. Magnasco, Philos. Mag. B **65**, 895 (1992).

[30] N. Rivier, J. Phys. (Paris) Colloq. **43**, C9-91 (1982); N. Rivier and R. Lissowski, J. Phys. A **15**, L143 (1982).

[31] J.J. Stoker, *Differential Geometry* (Wiley-Interscience, New York, 1969).